

# CONVECTIVE-REACTIVE PROTON-<sup>12</sup>C COMBUSTION IN SAKURAI'S OBJECT (V4334 SAGITTARII) AND IMPLICATIONS FOR THE EVOLUTION AND YIELDS FROM THE FIRST GENERATIONS OF STARS

FALK HERWIG<sup>1,8</sup>, MARCO PIGNATARI<sup>1,2,3,8</sup>, PAUL R. WOODWARD<sup>4</sup>, DAVID H. PORTER<sup>5</sup>, GABRIEL ROCKEFELLER<sup>6,8</sup>, CHRIS L. FRYER<sup>6,8</sup>, MICHAEL BENNETT<sup>7,8</sup>, AND RAPHAEL HIRSCHI<sup>7,8,9</sup>,  
 fherwig@uvic.ca  
 LA-UR 10-00630

## ABSTRACT

Depending on mass and metallicity as well as evolutionary phase, stars occasionally experience convective-reactive nucleosynthesis episodes. We specifically investigate the situation when nucleosynthetically unprocessed, H-rich material is convectively mixed with a He-burning zone, for example in convectively unstable shell on top of electron-degenerate cores in AGB stars, young white dwarfs or X-ray bursting neutron stars. Such episodes are frequently encountered in stellar evolution models of stars of extremely low or zero metal content, such as the first stars. We have carried out detailed nucleosynthesis simulations based on stellar evolution models and informed by hydrodynamic simulations. We focus on the convective-reactive episode in the very-late thermal pulse star Sakurai's object (V4334 Sagittarii). Asplund et al. (1999) determined the abundances of 28 elements, many of which are highly non-solar, ranging from H, He and Li all the way to Ba and La, plus the C isotopic ratio. Our simulations show that the mixing evolution according to standard, one-dimensional stellar evolution models implies neutron densities in the He intershell ( $\lesssim$  few  $10^{11}\text{cm}^{-3}$ ) that are too low to obtain a significant neutron capture nucleosynthesis on the heavy elements. We have carried out 3D hydrodynamic He-shell flash convection simulations in  $4\pi$  geometry to study the entrainment of H-rich material. Guided by these simulations we assume that the ingestion process of H into the He-shell convection zone leads only after some delay time to a sufficient entropy barrier that splits the convection zone into the original one driven by He-burning and a new one driven by the rapid burning of ingested H. By making such mixing assumptions that are motivated by our hydrodynamic simulations we obtain significantly higher neutron densities ( $\sim$  few  $10^{15}\text{cm}^{-3}$ ) and reproduce the key observed abundance trends found in Sakurai's object. These include an overproduction of Rb, Sr and Y by about 2 orders of magnitude higher than the overproduction of Ba and La. Such a peculiar nucleosynthesis signature is impossible to obtain with the mixing predictions in our one-dimensional stellar evolution models. The simulated Li abundance and the isotopic ratio <sup>12</sup>C/<sup>13</sup>C are as well in agreement with observations. Details of the observed heavy element abundances can be used as a sensitive diagnostic tool for the neutron density, for the neutron exposure and, in general, for the physics of the convective-reactive phases in stellar evolution. For example, the high elemental ratio Sc/Ca and the high Sc production indicate high neutron densities. The diagnostic value of such abundance markers depends on uncertain nuclear physics input. We determine how our results depend on uncertainties of nuclear reaction rates, for example for the <sup>13</sup>C( $\alpha$ , n)<sup>16</sup>O reaction.

*Subject headings:* stars: AGB and post-AGB — stars: abundances — stars: evolution — stars: interior — stars: individual (V4334 Sagittarii) — physical data and processes: hydrodynamics — physical data and processes: nuclear reactions, nucleosynthesis, abundances

## 1. INTRODUCTION

### 1.1. Convective-reactive phases of stellar evolution

In stellar evolution the nuclear time scale is usually much larger than the convective mixing time scale. However, this is not always the case. An example of stellar nucleosynthesis where nuclear reactions and convective mixing occurs on the same time scale are slow neutron capture process branchings (*s* process, Burbidge et al. 1957; Wallerstein et al. 1997) in

He-shell flash convection of Asymptotic Giant Branch (AGB) stars, such as the branching at <sup>128</sup>I (Reifarth et al. 2004). This situation is comparatively simple to simulate as the rapid nuclear reaction in question, the double-decay of <sup>128</sup>I, does not release any significant amount of energy. A post-processing approach of the standard stellar evolution calculation with some one-dimensional treatment of convection, like mixing-length theory (MLT), with time-dependent mixing gives a reasonable approximation of this situation.<sup>10</sup>

<sup>1</sup> Department of Physics & Astronomy, University of Victoria, Victoria, BC V8P5C2, Canada

<sup>2</sup> Joint Institute for Nuclear Astrophysics, University of Notre Dame, Notre Dame, IN 46556, USA

<sup>3</sup> TRIUMF, 4004 Wesbrook Mall, Vancouver, BC V6T2A3, Canada

<sup>4</sup> LCSE & Department of Astronomy, University of Minnesota, Minneapolis, MN 55455, USA

<sup>5</sup> Minnesota Supercomputing Institute, University of Minnesota, MN, USA

<sup>6</sup> Computational Computer Science Division, Los Alamos National Laboratory, Los Alamos, NM 87545, USA; Physics Department, University of Arizona, Tucson, AZ 85721, USA

<sup>7</sup> Astrophysics group, Keele University, Lennard-Jones Lab., Keele, ST55BG, UK

<sup>8</sup> NuGrid collaboration

<sup>9</sup> Institute for the Physics and Mathematics of the Universe, University of Tokyo, 5-1-5 Kashiwanoha, Kashiwa 277-8583, Japan

<sup>10</sup> Although even in this case multi-dimensional effects of convection have to be taken into account eventually as simulations by Herwig et al. (2006) indicate that the velocity profile at the bottom of the convective shell is flatter compared to the MLT prediction.

The goal of this paper is instead to investigate the situation when rapid nuclear reactions are indeed releasing amounts of energy that are likely to affect the fluid flow, as for example in the case of proton capture of  $^{12}\text{C}$  in convective He-burning. In the fluid dynamics community this mixing regime is sometimes referred to as level-3 mixing, where the flow is altered by attendant changes in the fluid (Dimotakis 2005). We refer to these situations as reactive-convective phases in order to emphasize the fact that the time scales of highly exothermic nuclear reaction and the convective fluid flow time scales are of the same order.

The ratio of the mixing time scale and the reaction time scale is called the Damköhler number:

$$D_\alpha = \frac{\tau_{\text{mix}}}{\tau_{\text{react}}} . \quad (1)$$

MLT is concerned with averaged properties both in time over many convective turn-overs and in space over the order of a pressure scale height. In the categories of Dimotakis (2005) diffusion coefficients derived from MLT may describe level-1 mixing (while mixing induced by rotation involves flow dynamics that are altered by mixing processes and labeled in this scheme as level-2 mixing). Therefore, time-dependent mixing through a diffusion algorithm with diffusion coefficients derived from MLT is appropriate for regimes with  $D_\alpha \ll 1$ . The difficulty of simulating convective-reactive phases in present one-dimensional stellar evolution codes then appears as the inability of MLT (or any similar convection theory) to properly account for the additional dynamic effects introduced through rapid and dynamically relevant nuclear energy release in level-3 mixing associated with Damköhler numbers  $D_\alpha \approx 1$ .

Convective-reactive episodes can be encountered in numerous phases of stellar evolution, including the He-shell flash of AGB stars of extremely low metal content (e.g. Fujimoto et al. 2000; Suda et al. 2004; Iwamoto et al. 2004; Cristallo et al. 2009), metallicity low-mass stars (e.g. Hollowell et al. 1990; Schlattl et al. 2002; Campbell & Lattanzio 2008), young white dwarfs of solar metallicity (e.g. Iben et al. 1983; Herwig et al. 1999; Lawlor & MacDonald 2003), both rotating and non-rotating Pop III massive stars (Ekström et al. 2008), and more in general, in low metallicity massive stars (Woosley & Weaver 1995). These combustion events are encountered as well in X-ray burst calculations of accreting neutron stars (Woosley et al. 2004; Piro & Bildsten 2007), and accreting white dwarfs (Cassisi et al. 1998) that may be the progenitors of SN Ia. Convective-reactive events have been found in post-RGB stellar evolution models and associated with the horizontal branch anomalies in certain globular clusters (Brown et al. 2001; Miller Bertolami et al. 2008). Finally, again in AGB stars, convective-reactive phases can be found in hot dredge-up (Herwig 2004; Goriely & Siess 2004; Woodward et al. 2008), a phenomenon that is associated with the treatment of convective boundaries, generally in more massive and lower metallicity AGB stars.

Although convective-reactive phases are quite common in stellar evolution, in particular in the early, low-metallicity Universe, we do not currently have a reliable and accurate way of simulating them. In this work we discuss the case of the He-shell flash with H-ingestion in a very-late (post-AGB) thermal pulse at solar metallicity. This situation is extremely similar to H-ingestion associated with the He-shell flash in AGB stars at extremely low metallicity. The one-dimensional, spherically-symmetric stellar evolution approximation is not very realistic in this case, because both the entrainment of H into the He-shell flash convection zone as well as the subsequent con-

vective transport, mixing and nuclear burning of hydrogen enriched fluid parcels are inherently a three-dimensional hydrodynamic process. The energy from proton captures by  $^{12}\text{C}$  via the  $^{12}\text{C}(p, \gamma)^{13}\text{N}$  reactions is released on the same time scale ( $\sim 1 \dots 10 \text{min}$  for  $T = 1.3 \dots 1.05 \times 10^8 \text{K}$ ) of the fluid flow of convection (Sect. B), and this energy will add entropy to fluid elements and in turn feedback into the hydrodynamics (Herwig 2001). These highly coupled, multi-dimensional processes are approximated in through the MLT, complemented with a time-dependent mixing algorithm. This assumption may not be realistic in the present case (see Sect. 3.2 and 4.2).

## 1.2. Post-AGB flash star Sakurai's object and its observed abundance properties

Sakurai's object is a very-late thermal pulse post-AGB object (Duerbeck et al. 2000, and ref. there) and has experienced a H-ingestion flash in 1994. The star's observed abundance signatures are highly non-solar, and very unusual for a post-AGB low-mass star (Sect. 3.2). Nevertheless, there is wide agreement in the literature that the object's distance is 2–5kpc and that it has a mass of around  $0.6M_\odot$  (van Hoof et al. 2007, and ref. therein), pointing to a low mass star progenitor. Moreover, the high abundance of Li requires the existence of  $^3\text{He}$  in the envelope (Herwig & Langer 2001), pointing again to a low mass star progenitor that was not affected by hot bottom burning (HBB). Indeed, hot-bottom burning occurs at solar metallicity for stars with  $M_{\text{ZAMS}} \gtrsim 4M_\odot$  and destroys  $^3\text{He}$  in the AGB envelope (Scalo et al. 1975). Another process, that could effect the evolution of  $^3\text{He}$  during the progenitor evolution of Sakurai's object is extra-mixing below the convective envelope during either the RGB or AGB (e.g. Wasserburg et al. 1995; Charbonnel & Zahn 2007; Denissenkov 2010). Sakurai's object serves potentially as an important constraint for theories of such mixing because the observed Li abundance increase during the observations in 1996 as reported by Asplund et al. (1999) can only be modeled in the very late thermal pulse if significant amounts of  $^3\text{He}$  are still present in the envelope at the beginning of the post-AGB evolution.

The light curve of this object was closely monitored as it evolved within approximately 2yr from the pre-WD location in the HRD back to the AGB location, a much shorter evolution time scale than previously predicted (Herwig et al. 1999). A possible explanation of such a fast born-again evolution of Sakurai's object is that the convective mixing efficiency in the He-shell flash convection zone is smaller by a factor of  $\sim 30$  compared to the MLT predictions in standard one-dimensional stellar models (Herwig 2001). This modification is motivated by the reasoning that in the convective-reactive regime the fluid flow would be eventually strongly affected by the energy released rapidly on a time scale comparable to the fluid flow velocity. This process, indeed, would locally add buoyancy to the fluid element causing a behavior that is not reflected in the mixing-length theory.

Miller Bertolami et al. (2006) have presented a more detailed investigation and emphasize the importance of appropriate time resolution. In addition, they studied the role of overshooting and  $\mu$ -gradients. Their simulations with exponential, depth-dependent overshooting agree better with observations than tracks computed without any overshooting.  $\mu$ -gradients appear to have only secondary effects. Confirming the mass dependence of the proton-ingestion born-again evolution first reported by Herwig (2001), Miller Bertolami & Althaus (2007)

point out that the initial return light-curve of Sakurai's object could be reproduced with a slightly lower mass model than the  $0.604M_{\odot}$  adopted by Herwig (2001), a high time resolution and their alternative description of convective transport. However, the second heating phase into which the Sakurai's object has entered now (van Hoof et al. 2007), seems to be better in agreement with the modified convection models proposed by Herwig (2001).

While the light curve of Sakurai's object has certainly raised doubts about the capability of one-dimensional stellar evolution calculations to reproduce its evolution, in this work we show that the abundance determinations by Asplund et al. (1999) pose a much more stringent constraint on the physics of convective-reactive phases. Asplund et al. determined 28 elemental abundances at four times between April and October 1996, when the star had cooled to below 8000K. In particular, among light elements a significant enhancement (at least 0.5 dex) with respect to the solar abundance has been observed for Li, Ne and P. Beyond iron, Cu, Zn, Rb and Sr peak elements are significantly enhanced. In addition, there are trends as a function of time that are smaller than the differences to solar. However, for this initial analysis which is not yet based on full hydrodynamic simulations with nuclear burn, we will not discuss those trends in detail.

A few preliminary comments on individual elements may be in order. The observed Li is clearly produced above the meteoritic value. Herwig & Langer (2001) proposed that together with protons  ${}^3\text{He}$  is ingested into the He-shell flash convection zone, providing the fuel to produce Li via the reaction chain  ${}^3\text{He}(\alpha, \gamma){}^7\text{Be}(\beta^+){}^7\text{Li}$ . The first *s*-process peak elements are enhanced by up to 2dex while Ba and La are not enhanced, causing a ratio of Ba peak to Sr peak elements that is much lower than expected from models and observations of AGB stars (Busso et al. 2001). We can translate the abundances observed by Asplund et al. (1999) into the ratio of the two *s*-process indicator indices *hs* and *ls*. An *s*-process index  $s/s_{\odot}$  is the overproduction factor of a group of *s*-process elements with respect to the initial solar value. The index ratio  $[\text{hs}/\text{ls}] = [\text{hs}/\text{Fe}] - [\text{ls}/\text{Fe}]$  monitors the distribution of the *s*-process elements, and it is an intrinsic index of the neutron capture nucleosynthesis on heavy elements (Luck & Bond 1991). We have used  $[\text{ls}/\text{Fe}] = \frac{1}{3}([\text{Sr}/\text{Fe}] + [\text{Y}/\text{Fe}] + [\text{Zr}/\text{Fe}])$  and  $[\text{hs}/\text{Fe}] = \frac{1}{2}([\text{Ba}/\text{Fe}] + [\text{La}/\text{Fe}])$ , where square brackets indicate the logarithmic ratio with respect to the solar ratio (Table 1). For Asplund's October measurements the indices are  $[\text{hs}/\text{Fe}] = 0.05$  and  $[\text{ls}/\text{Fe}] = 1.9$  assuming that  $[\text{Fe}/\text{H}] = 0.0$  for Sakurai's object. We record measurements of  $\pm 0.2 \dots 0.3$  dex as the average approximate index ratio  $[\text{hs}/\text{ls}] \sim -2$  at the end of the observed period. In Fig. 1, we compare such ratio with *s*-process theoretical predictions and stellar observations of low mass AGB stars, that are the progenitor population of the Sakurai's object. In particular, we show that the observed  $[\text{hs}/\text{ls}]$  is a factor of ten or more lower than in typical AGB stars. Therefore, the nucleosynthesis environment that has generated the abundances observed by Asplund et al. was very different from that encountered in the previous AGB phase. In Fig. 1 we also include  $[\text{hs}/\text{ls}]$  from our nucleosynthesis calculations presented in this paper, that successfully reproduce the same ratio measured in the Sakurai's object. Such calculations will be discussed in detail in Section 5.

The abundance pattern of Sakurai's object further distinguishes itself from the AGB stars through the significantly en-

hanced P, Cu and Zn. These elements are not usually produced in low-mass stars. Several other elements are reduced, i.e., S, Ti, Cr and Fe. In particular, Fe is expected to be depleted, since it is the seed for *n*-capture nucleosynthesis. All these abundance signatures appear to be the result of a *n*-capture burst of large *n*-density. Another important feature is the C isotopic ratio  ${}^{12}\text{C}/{}^{13}\text{C} \sim 3-4$ , where the large  ${}^{13}\text{C}$  abundance results from the  ${}^{12}\text{C}(p, \gamma){}^{13}\text{N}(\beta^+){}^{13}\text{C}$  reaction channel.  ${}^{13}\text{C}$  is also the main neutron source during the H ingestion event, which causes the peculiar abundance signature observed by Asplund et al. (see Section 5 for details).

In the following we will briefly describe the tools we use in this investigation (Sect. 2) and defer more details to an appendix (Sect. A). Next we describe the stellar evolution picture of Sakurai's object and show how nucleosynthesis simulations based directly on the output of one-dimensional stellar evolution calculations fail to account for the observed abundance patterns (Sect. 3). Then we describe hydrodynamic simulations of entrainment into He-shell flash convection that motivate our modified mixing assumptions (Sect. 4). We will show how corresponding nucleosynthesis simulations account for the observed abundances, and we discuss the influence of nuclear reaction rate uncertainty (Sect. 5). The paper ends with a summary and some remarks on implications for the nucleosynthesis in the first generations of stars, including the light-element primary process (Sect. 6). In the appendix we give additional information on the codes we have used, and in Appendix B we discuss time scales for burning and mixing.

## 2. SIMULATION CODES

Three different types of simulation codes have been used in this work:

- a stellar evolution code (EVOL), providing one-dimensional stellar evolution up to the post-AGBn and thermodynamic structures for the beginning of the post-AGB He-shell flash event, also known as the very late thermal pulse (VLTP);
- a multi-zone post-processing nucleosynthesis code (PPN) with complete nuclear network and mixing;
- a multi-dimensional-hydrodynamical code (PPM), to study how hydrogen is ingested during the VLTP.

We have used the stellar evolution code EVOL to calculate the global evolution of post-AGB stars (Sect. 3.1) experiencing a VLTP (Blöcker 1995; Herwig 2000; Herwig & Austin 2004). The assumptions and input physics choices are very similar to those in Herwig (2001). Furthermore, we have used structures from the last thermal pulse of the AGB model by Herwig & Austin (2004), and of the VLTP model by Herwig et al. (1999).

For the detailed nucleosynthesis simulations (Sect. 3.2 and 5) we have used the PPN (Post-Processing Nucleosynthesis) code (Herwig et al. 2008). This code allows to calculate the complete nucleosynthesis along the radial profile of a star according to the structure input from a stellar evolution model in as many zones as required. Nuclear burn steps are alternated with time-dependent mixing steps. Details, including the nuclear physics data information, are given in Sect. A.1.

In order to investigate the hydrodynamic behaviour of unprocessed H-rich material entrained into the He-shell flash convection (Sect. 4), we used Woodward's PPM gas dynamics code with the PPB advection scheme on a cartesian grid (Woodward

et al. 2003, 2006; Woodward et al. 2008). For important code details, see Sect. A.2.

### 3. THE STELLAR EVOLUTION PICTURE

#### 3.1. Global stellar evolution scenario and calculation

The VLTP evolution scenario involves a He-shell flash on a single young white dwarf after the end of H-shell burning when the evolution track has just entered the white dwarf cooling curve in the HRD, as for example shown in Herwig et al. (1999), and in more detail in Sect. 3.2.1 of Miller Bertolami et al. (2006). It involves the convective ingestion of all or parts of the small ( $\sim 10^{-4}M_{\odot}$ ) remaining unprocessed, and thus H-rich, envelope into the hot ( $T = 1 \dots 3 \times 10^8$  K) He-burning flash layers. This He-burning convection zone contains a mass fraction of 20...40% (depending on convective model assumptions, Herwig 2000; Miller Bertolami et al. 2006) of primary  $^{12}\text{C}$ . Protons are rapidly captured by the abundant  $^{12}\text{C}$ , on the time scale of convective fluid flows of approximately 5...10min.

The progenitor is a low mass AGB star for which *s*-process element enhancements are expected at the Sr-Y-Zr peak and at the Ba peak (e.g. Busso et al. 2001). elements signature observed in Sakurai's object is not typical of the *s* process in AGB stars. Indeed, according to the observations by Asplund et al. (1999), the ratio of the second peak to the first peak *s*-process elements is  $[\text{Ba}/\text{Y}] \sim -2$ , in contrast to the expected AGB stars ratio  $-1 < [\text{hs}/\text{ls}] < 1$  at solar-like metallicity (e.g. Busso et al. 2001). This result does not change if we assume a lower than solar metallicity for Sakurai's object of  $[\text{Fe}/\text{H}] = -0.63$  (values between brackets in Tab.1). Such a choice may be indicated by the sub-solar observed Ba abundance, and indeed, the Ba and La abundance even lead us to assume that there was no significant *s*-process contribution in the previous AGB phase at all.

In any case, the peculiar abundance signatures of Sakurai's object has to originate in the H-ingestion event of the VLTP, and can not be explained in terms of any nucleosynthesis during the AGB progenitor evolution.

The initial abundance distribution for our post-AGB He-shell flash nucleosynthesis simulations is a combination of light elements (with  $A < 23$ ) from the intershell abundance of an AGB star at the end of the evolution taken from a  $2M_{\odot}$  simulation similar to those in Herwig & Austin (2004), and heavier species according to Asplund et al. (2005) with the isotopic ratios from Lodders (2003) scaled to metallicity  $[\text{Fe}/\text{H}] = -0.18$ .

The intershell abundances that matter for our simulations are mostly primary He-burning products, so details of the initial abundance are not important. The choice of more recent solar abundances (Asplund et al. 2009; Lodders et al. 2009) would not modify the results presented in this paper.

In the following section we will discuss the nucleosynthesis according to one-dimensional stellar evolution mixing predictions of the very-late thermal pulse.

#### 3.2. Nucleosynthesis according to the stellar evolution model

Fig. 2 shows the H-profile from stellar evolution in the initial phase of the H-ingestion phase for a model like those in (Herwig 2001), recalculated with  $f_v = 30$  and higher time resolution. The proton abundance at any location is the result of mixing and simultaneous burning. The two times correspond to panel A and B in Fig. 4 in Miller Bertolami et al. (2006) and the account of events given in their Sect. 3.2.1 applies here as well.

At time  $t_0$  the He-shell flash convection zone is about to make contact with the H-rich layers above. The H-profile at  $m_r \sim 0.6042M_{\odot}$  is the burning profile of the now extinct H-shell. During the late phase of the post-AGB evolution, basically past the 'knee' in the HRD, the H-shell is inactive, and the He-shell convection can grow into the H-rich layers and mix those protons (and  $^3\text{He}$ ) down into the  $^{12}\text{C}$ -rich He-shell flash convection zone. As H is mixed into deeper and hotter regions its lifetime against capture by  $^{12}\text{C}$  decreases because the rate of the nuclear reaction  $^{12}\text{C}(p, \gamma)^{13}\text{N}$  increases strongly with temperature. At some depth, in our simulation at  $m_r = 0.6005M_{\odot}$ , the mixing time scale equals the nuclear time scale (Damköhler number  $Da \sim 1$ , Sect. 1.1) and protons are now reacting rapidly with  $^{12}\text{C}$ , thereby releasing for a brief period more energy than the He-shell that is initially driving the flash.

In the stellar evolution simulation we treat time-dependent mixing mathematically as a diffusion process. It is implicitly assumed that on spheres the H-abundance is exactly homogeneous, and that the radial mixing efficiency based on the radial mean convective velocity is also exactly homogeneous. This assumption in combination with the strong temperature sensitivity of the p-capture reaction causes the stellar evolution code to predict the shell of peak H-burning energy release to be extremely thin. In the stellar evolution code an entropy step develops that separates the H-ingestion top convection from the He-shell flash convection underneath. A thin radiative zone formally prohibits mixing between the two convection zones. It shows up as a break in the diffusion coefficient line for time  $t_1$  in the top panel of Fig. 2. It now depends on the convective boundary mixing assumptions whether or not material from the top convection zone can mix below and vice versa. These boundary mixing assumptions, i.e. the amount of overshooting appropriate for this situation, is not yet known.

Fig. 2 shows that the split of the two convection zones appears already very early when only a small amount of protons has been consumed. We mark the position in the H-profile and the corresponding H-abundance that has been reached at the time when the split occurs in the lower panel. The good agreement of our evolution simulation with the result by Miller Bertolami et al. (2006, Fig. 3 in their work) only means that these calculations properly converge and are precise, but not that they are accurate.

At the time of the split the peak temperature in the now separated top H-burning driven convection zone is  $T \lesssim 1.0 \times 10^8$  K. Although the  $^{12}\text{C}(p, \gamma)^{13}\text{N}(\beta^+)^{13}\text{C}$  reaction chain is providing plenty of the neutron source isotope  $^{13}\text{C}$ , the  $^{13}\text{C}(\alpha, n)^{16}\text{O}$  reaction activation depends on the peak temperature reached in this top convection layer. For  $T = 10^8$  K the lifetime of  $^{13}\text{C}$  against capture by  $^4\text{He}$  (and thus the time-scale of releasing neutrons) is 454yr, and thus *neutron capture nucleosynthesis is negligible*, considering that the born-again life time is only a few years. As a result, these stellar evolution models cannot provide the environment to generate abundance patterns as observed by Asplund et al. (1999).

We have performed a full nucleosynthesis analysis of the stellar evolution model sequence shown in Fig. 2, using the MPPNP code (Sect. A.1). The technique for this nucleosynthesis analysis is explained in full detail in Sect. 5. Indeed no modification of heavy element abundances is seen, in disagreement with the observations by Asplund et al. (1999), and in agreement with the qualitative arguments that these authors made in their original paper.

The Herwig et al. (1999) models show a larger peak-temperature of  $T = 1.5 \times 10^8 \text{ K}$ <sup>11</sup> for the H-ingestion driven top convection zone. As discussed in detail in Herwig (2001), those older models are not correctly reproducing the fast luminosity rise time observed in Sakurai's object, and it exists an inverse correlation between the rise time and the depth of the burning zone and split (i.e. convection speed, peak temperature). models with the higher peak temperature have far too slow rise times and can thus be excluded. For these higher peak temperatures the life time of  $^{13}\text{C}$  is 0.13 yr. However, even this is not short enough to generate the abundance patterns observed in Sakurai's object (see Sect. 5 for further discussion).

We conclude from this analysis that a one-dimensional stellar evolution calculation cannot fully account for the mixing conditions in the convective-reactive H-ingestion flash that occurred in Sakurai's object. In this section we have already hinted at the possible reasons for the discrepancy. We will now have a closer look at what information and guidance we can derive from present three-dimensional hydrodynamic simulations of He-shell flash convection.

#### 4. THE HYDRODYNAMIC PICTURE

##### 4.1. *New simulations*

In order to study the hydrodynamic process of entrainment and further mixing of H-rich material from the stable layers into the convection zone we have carried out new gas dynamics simulations of the entire three-dimensional He-shell flash convection domain in  $4\pi$  geometry (Fig. 3). We used the PPM code described in Sect. A.2. We have not included burning of protons with  $^{12}\text{C}$  because we restrict the goal of the numerical experiments purely to the investigation of mixing properties during the onset of the H-ingestion, which starts when the He-shell flash convection has reached its largest Lagrangian extension.

Herwig et al. (2006) simulated the He-shell flash convection shell as plane-parallel box-in-a-star. They selected an earlier phase of the He-shell flash when the convection had not yet reached its largest extent, and the H-rich layers had not been reached. Therefore only  $\sim 4.5$  pressure scale heights needed to be included in those simulations which made them considerably less demanding than the new simulations. In addition the previous simulations were only in 2D.

The new simulations were performed on a cubical domain with two uniform Cartesian grids of  $576^3$  and  $384^3$  respectively (Fig. 3).<sup>12</sup> Each simulation realistically represents the abundance mixture in the He-shell flash convection zone and in the stable layer above as different materials with the correct molecular weight ratio. The setup includes an inert white-dwarf-like core and a radiative region below the bottom of the He-shell flash convection zone at 9,500km where the gravitational acceleration is  $4.9545 \cdot 10^7 \text{ cm/s}^2$ , the density is  $1.174 \cdot 10^4 \text{ g/cm}^3$  and the pressure is  $1.696 \cdot 10^{20} \text{ g/cm}^2$ . At the bottom of the convection zone a luminosity of  $4.2 \cdot 10^7 L_\odot$  is artificially added in a shell of 1,000km. This heating corresponds to the He-burning that drives the flash, and compares as follows to the He-shell flash luminosity in the stellar evolution models shown in Fig. 2. In the model at time  $t_0$  the He-burning luminosity is at its peak

of  $L_{\text{He},0} = 4.75 \cdot 10^7 L_\odot$  whereas it drops somewhat once the H-burning flash ignites at  $t_1$  when  $L_{\text{He},1} = 4.27 \cdot 10^7 L_\odot$ . Thus, the 3D hydrodynamic simulations are driven at the nominal heating rate.

The top of the convection zone is at a radius of 30,000km and surrounded by a radiative shell of thickness 4,500km. The three layers are each polytropes. The adiabatic polytrope that represents the convection zone spans  $\sim 9H_p$ . The setup contains two materials. The lighter material represents the H/He mixture in the stable layer above the convection zone. The heavier fluid represents the  $^{12}\text{C}$ -rich mixture that occupies the convection zone. We have assumed here that the material in the stable layer below the convection zone has the same molecular weight. The ratio of the molecular weights of the two components is  $\mu_{\text{C,O,He}}/\mu_{\text{H,He}} = 2.26$ .

The higher resolution run (Fig. 3, right panel) is shown at time 21,653s. For convective transport the typical radial velocities are of interest. In the shown snapshot the largest radially rms-velocities are found about 4,500km above the bottom of the convection zone around  $\langle v_{\text{rad,ave}} \rangle = \sqrt{2} \langle E_{\text{kin}} \rangle \sim 12.5 \text{ km/s}$ . The velocity of individual convective gusts can be significantly higher. Towards the upper boundary of the convection zone the radial velocities decrease to a few km/s. This is compensated by large tangential velocities  $> 12 \text{ km/s}$  which stay this high all the way to the convection boundary (Fig. 4). The resulting strong radial gradient of the tangential velocities at the top convection boundary is, via Kelvin-Helmholtz instabilities, likely the main mechanism of the entrainment and convective boundary mixing that we observe in these simulations. The information on typical convective velocities together with the radial scale of the convection zone implies a convective turn-over time scale of the order  $\sim 3000\text{s}$  (cf. Appendix B). Therefore, Fig. 3 shows the entrainment after  $\sim 7$  convective turnovers.<sup>13</sup> When estimating the time scale for H-rich material to enter the convection zone it must be considered that the entrained material is dominantly transported in downflow lanes that are gravitationally compressed as the material descends. This mechanism is reflected in the radial velocities of the H-rich material that has entered the convection zone, which in the snapshot shown exceed  $20 \text{ km/s}$ . We note that for this component even the radially averaged velocity corresponds to a Mach number  $Ma \sim 0.02$  which is much higher than the MLT convective velocity based estimate of  $Ma \sim 0.001$ .

After some initial transient period the convection assumes a flow pattern that is dominated by large upwelling convective cells that occupy typically a full octant as they emerge at the top convection boundary. These large convective structures can be observed because we simulate the full  $4\pi$  sphere. Entrainment of the H-rich material from the stable layer into the convection zone is mostly associated with downdraft lanes that form when large cells collide on the surface of the convection zone (Fig. 3). Note that the radially averaged profile of the ingested H-rich material from the 3D hydro-simulation is qualitatively very similar compared to the diffusion picture of the one-dimensional stellar evolution (Fig. 5), at least close to the upper boundary. Further inward the lines divert from each other systematically as no H is burned in the 3D simulations (this

<sup>11</sup> We have now recalculated those old models with higher resolution and find the peak H-burning location at slightly lower temperature of  $T = 1.3 \times 10^8 \text{ K}$ .

<sup>12</sup> The  $576^3$  calculation took 4 days on 24 workstations at the University of Minnesota's Laboratory for Computational Science & Engineering (LCSE). A movie made from the output of this run may be downloaded from the LCSE Web site.

<sup>13</sup> We have continued this run for another 14 convective turnovers. However, as will become clear from the following discussion the omission of proton burning limits the scientific use of that later part of the run to our application. Note that the time step of the 3D simulations is limited to  $\Delta t = 5.9 \cdot 10^{-2} \text{ s}$  which implies that 300,000 cycles had to be computed to reach the state shown.

physics is not yet included).

However, the important result of the 3D simulations is that entrainment is rather inhomogeneous and asymmetric, as well as intermittent in locally confined wedges of the star. From the snapshot image of the entrainment it is clear that significant anisotropy of the H-abundance is advected into the deeper layers where the burning will eventually take place.

#### 4.2. Implications for the nucleosynthesis in a convective reactive environment like Sakurai's object

We will give a full account of these simulations elsewhere. Here we want to describe a few properties that are relevant for guiding our mixing strategy for the nucleosynthesis simulation of the flash in Sakurai's object. The details of the convective-reactive burning of hydrogen in the He-shell flash convection zone depend on two aspects of the problem that hydrodynamic simulations can address. The first is the process of entrainment. How much is the fuel is premixed immediately after the entrainment in the near-boundary layers. Subsequently these H-enriched fluid elements will be carried along with the convective flow to deeper and hotter layers where protons will eventually react with  $^{12}\text{C}$ . This leads to the second aspect of the problem, the hydrodynamic feedback of the nuclear energy released. In the one-dimensional simulations this feedback is in the form of a sharp entropy barrier, or a thin shell of positive entropy gradient locally confined to a sphere. In reality the thickness of this layer will depend on the velocity distribution and the abundance distribution of fluid elements entering the layers hot enough for rapid burning.

We can illustrate the possible outcomes by considering two extreme cases. Assuming first that any entrained material is immediately mixed and that vertical velocities of fluid elements are only deviating negligibly from some average value (obviously, this case is very close to the MLT picture of convection) then all fluid parcels or blobs would release nuclear energy at almost the same radial position inside the convection zone, and thus a very thin burn layer would form, concentrating the entropy jump into a narrow region with large positive entropy gradient, and soon inhibiting any further radial mixing. The other extreme would be a wide range of mixing ratios in blobs of H-enriched material entering the deeper layers with a large range of velocities. Both of these inhomogeneities lead to a broadening of the burning layer. To first approximation a blob (note that this may be a shredded blob in order to conceptually overcome mixing-length concepts) burns at  $Da \sim 1$  (Sect. 1.1). For smaller  $Da$  (above the burning layer) the nuclear reaction time scale is longer than the mixing time scale and the blob will rather move further down than burn. For  $Da > 1$  we are below the burning layer because now the blob burns faster than it can move further down. Since the burn time scale decreases with depth a range of mixing velocities translates into a spatial range in which  $Da \sim 1$ . Differently than in the first case, the velocity distribution of blobs leads to a broadening of the burn layer. Distributing the energy released from proton capture over a thicker layer will make the emerging entropy gradient shallower. Mixing across the burn layer will be more efficient. A distribution of levels of H-enrichments in blobs being advected through the burn layer would mean that the H-abundance is heterogeneous (patchy) on spheres. Thus, the energy generation and the dynamic feedback may very well be patchy and inhomogeneous on spheres, as well as time variable. At least initially, the inhibiting effect of the burn layer on mixing may as

well be time variable and inhomogeneous on spheres.

In other words, an inhomogeneous distribution of fuel abundance in blobs together with a distribution of vertical blob velocities would have the tendency to delay the inhibiting effect of nuclear burning on mixing from the top to the bottom of the convection zone. We leave a detailed quantitative analysis of these processes to a forthcoming investigation. Here we focus on the conceptual guidance we can gain from the hydrodynamic simulations. These do indeed show a significant inhomogeneity of the entrained material all the way down to the bottom of the convection zone (Fig. 3), as well as a significant distribution of vertical velocities, including convective gusts up to Mach numbers around  $Ma \sim 0.03$ .

We conclude from this analysis that the hydrodynamic nature of the convective-reactive phase of H-ingestion into the He-shell flash convection zone likely translates into a continued mixing through the burn layer. We therefore hypothesize that mixing is not inhibited at the early stage, as indicated by stellar evolution models, but that instead mixing across the H-burning layer is possible for a prolonged period. It may stop only at a later time after more H-ingestion has taken place. In the next section we will test this hypothesis through nucleosynthesis simulations that can be compared with the observations Asplund et al. (1999).

## 5. NUCLEOSYNTHESIS SIMULATIONS

In this section we will describe mixing and nucleosynthesis simulations based on the thermodynamic stellar evolution structure of a post-AGB He-shell flash. We describe initially two cases, one that resembles the mixing predicted by stellar evolution (Sect. 5.2), and one with a mixing prescription that reflects the findings discussed in the previous section (Sect. 5.3). While the first fails to reproduce key observational features of Sakurai's object, the second one succeeds. We show that high neutron densities in the range  $10^{12} < N_n/\text{cm}^{-3} < 10^{16}$  are required to reproduce the observed abundance features, as already pointed out by Asplund et al. (1999). Such a neutron density regime is higher than the classic *s* process and significantly lower compared to the classic *r* process.

### 5.1. General setup of nucleosynthesis simulations

We are using the MPPNP post-processing code (Sect. A.1) to calculate the nucleosynthesis of a He-shell flash peak one-dimensional stellar structure model. We use two structures, one of them shown in Fig. 2 for  $t = t_0$ . The MPPNP code reads the mixing-length theory diffusion coefficient as well as the temperature and density structure from the stellar evolution structure model. We post-process this structure with sub-time steps of  $\Delta t_{\text{post-processing}} = 63\text{s}$ . Thus, the mixing time scale is well resolved, and the numerical splitting of the mixing and the nucleosynthesis operators is justified. The He-shell flash convection zone is spatially resolved with 70 to 90 zones. The grid is statically refined and provides extra resolution near the ingestion layer at the top of the convection zone, as well as around any split region, should it be included.

The MLT based diffusion coefficient that is read in along with the stellar structure from the stellar evolution output does not show a split because the stellar evolution model is from a time just before the ingestion of H-rich material begins. However, we are providing for an optional split that can be inserted at an arbitrary location and time, by modifying the diffusion

coefficient in Eulerian coordinates in the following way

$$D_{\text{with split}} = \frac{D_{\text{MLT}}}{(1 + a_2 \exp(-a_1(m_r - m_{r,\text{split}}))^2)} \quad (2)$$

where the split is located at  $m_{r,\text{split}}$ . When a split is imposed it is chosen to be deep enough so that only very little material can be mixed through, and the split is also very narrow. With  $a_1 = 10^4$  and  $a_2 = 10^7$  the diffusion coefficient in the convection zone of  $D_{\text{MLT}} \sim 5 \cdot 10^{13} \text{cm}^2/\text{s}$  is reduced to  $D_{\text{split,min}} \sim 5 \cdot 10^6 \text{cm}^2/\text{s}$  over a width of  $< 10^{-4} M_\odot$ . We emphasise that  $a_1$  and  $a_2$  are free parameters of our simple delayed split model and their particular value is not important at this point. Only further hydrodynamic simulations can possibly determine the mixing properties in this environment. The purpose of the delayed split in terms of the radially averaged nucleosynthesis calculations is further discussed below.

We are solving only for the nucleosynthesis and mixing equations while the  $T$ ,  $\rho$  stratification is assumed to remain unchanged. Protons and  $^3\text{He}$  are inserted into the top of the convection zone at a rate that is derived from the Lagrangian velocity of the top of the convective boundary, as it moves into the H-rich layers above the convection zone in the stellar evolution model. This velocity is  $\dot{M}_{\text{top,conv}} \sim 1.7 \times 10^{-2} M_\odot/\text{yr}$ . We are ingesting at a rate of  $5.3 \times 10^{-10} M_\odot/\text{s}$ .<sup>14</sup> We also add  $^3\text{He}$  according to the solar H/ $^3\text{He}$  ratio in order to obtain a prediction for Li.

Another constraint is that the total amount of H available for ingestion is limited to the small remaining envelope mass that remains on the pre-formed WD when the star leaves the AGB. For a core mass of  $0.6 M_\odot$  this envelope mass is  $\sim 10^{-4} M_\odot$  with H and He fractions as expected at the end of the AGB (mostly the initial ratio possibly modified by third dredge-up). In all of the cases discussed here we always find a nucleosynthetic reason to stop a simulation before we run out of fuel.

### 5.2. Stellar evolution mixing case

In the stellar evolution models the convection zone split due to H-burning activation starts as soon as H is ingested (Sect. 3.2), and no H or  $^{13}\text{C}$  can be mixed below the split coordinate. In Fig. 6, we show the abundance distribution prediction at the top of the convection zone for this model in comparison with the observations by Asplund et al. (1999). We have used the  $(\rho, T, D)$  stratification (strat-A) from the (Herwig et al. 1999) sequence, selecting a model just before the H-ingestion starts as a template for this run. The mixing split as described in the previous section is activated immediately as H starts to mix into the convection zone. Peak H-burning is located at a higher temperature in the (Herwig et al. 1999) sequence compared to more recent models, and therefore this case yields an upper limit of the nucleosynthesis efficiency predicted from one-dimensional models.<sup>15</sup>

Calculations are run for about one year, after which also Ba starts to be produced, in disagreement with observations. The neutron density reaches a value of the order of  $10^{11} \text{cm}^{-3}$  at the split coordinate due to the high  $^{13}\text{C}$  concentration accumulated via proton capture on  $^{12}\text{C}$ . This value is comparable with the neutron density obtained at the bottom of a regular He-shell

flash convection zone from  $^{22}\text{Ne}(\alpha, n)^{25}\text{Mg}$  reaction. Nevertheless, the predicted abundances do not matching the observations.

Li was produced initially during the ingestion (see below and Herwig & Langer 2001, for more details) is destroyed on the time scale of  $\sim 1$  yr. Stellar models predict that material around and beyond the split expands and cools which reduces the  $\alpha$ -capture efficiency depleting Li. But this also reduces the production of heavy elements.

Sc is well reproduced within the uncertainties, in neutron densities higher than in the classic  $s$ -process.  $^{40}\text{Ca}$  is the main seed along the neutron capture path, and Sc is mainly produced as  $^{45}\text{Ca}$  which will decay to  $^{45}\text{Sc}$  in  $\sim 166$  days. The production of Sc is subject to nuclear reaction uncertainties, for instance the  $(n, \gamma)$  rates of Ca isotopes,  $^{41}\text{Ca}(n, p)^{41}\text{K}$  and in particular  $^{41}\text{Ca}(n, \alpha)^{38}\text{Ar}$ .

The bottom line is that Li observations cannot be reproduced together with a significant  $s$ -process nucleosynthesis in this simulation. But most importantly, the predicted [hs/lr] ratio much higher than observed. Therefore, the nucleosynthesis simulation based on the one-dimensional stellar evolution prediction for mixing cannot account for the observed abundance patterns in Sakurai's object, which confirms our findings from Sect. 3.2.

### 5.3. Delayed split model motivated by the hydrodynamic simulations

We now assume that the split is not created instantaneously by H-burning, but mixing continues — at least initially — unrestricted despite the energy generation from H-burning (see Sect. 4.2). We use same background model (strat-A) as in Sect. 5.2.

$^{13}\text{N}$  is still formed in the upper layers where the reaction and the mixing time coincide (Fig. 7).  $^{13}\text{N}$  decays to  $^{13}\text{C}$  on a time scale of  $\sim 10$ min. During this time  $^{13}\text{N}$  will be swept along with the flow, possibly covering a distance of the order 10,000km. Eventually  $^{13}\text{C}$  is mixed to the bottom of the He-shell flash convection zone ( $T \sim 2.5 - 3.0 \cdot 10^8$  K) and establishes an abundance of  $\sim 1\%$  by mass throughout the He intershell. Neutrons are released via  $^{13}\text{C}(\alpha, n)^{16}\text{O}$  on the time scale of 1...10s and neutron densities reach a value of  $\sim 10^{15} \text{cm}^{-3}$  at the bottom of the convection zone. The profile for Sr is shown as an example for how the abundance, even of heavy elements, varies inside the convection zone as mixing and production proceed at similar time scales.

The intense neutron burst leads to the formation of the first  $s$ -process peak elements Rb, Y, Sr, Zr, with Fe as the main seed. The unimpeded mixing between the formation region of  $^{13}\text{N}$  and the deeper layers where the neutrons are released must finish before the Ba-La elements are significantly produced, which is not observed. This defines the moment when mixing finally has to be limited, and we then turn on the delayed split. In Fig. 8 we show the abundances expected at the top of the He intershell for different split time between 800min to 1200min.

Burning of  $^3\text{He}$  produces  $^7\text{Be}$  via the reaction  $^3\text{He}(\alpha, \gamma)^7\text{Be}$ , which will decay later to  $^7\text{Li}$ . As pointed out by Herwig & Langer (2001), Li destruction is avoided under these conditions not because Li is mixed into cooler regions (Cameron-Fowler

<sup>14</sup> Specifically, we add every  $\sim 6$ min (every 6<sup>th</sup> cycle, corresponding roughly to 10 times per convective turn-over time)  $\Delta X = 5 \times 10^{-4}$  to the mass fraction of H in the uppermost  $4 \times 10^{-4} M_\odot$  of the convection zone. The baryon numbers are conserved by subtracting the required mass fraction from  $^{12}\text{C}$ . The abundances up to  $^{23}\text{Na}$  are initialized as described in Sect. 3.1.

<sup>15</sup> As discussed in Sect. 1.2 this older model did not reproduce the observed light curve, but more recent models Herwig (2001); Miller Bertolami et al. (2006) predict the split at lower temperature and as a result even less n-induced nucleosynthesis.

mechanism). Rather, in this *hot H-deficient  $^3\text{He}$ -burning* all the protons are consumed before  $^7\text{Be}$  decays to  $^7\text{Li}$ . Then  $^7\text{Li}$  is more stable as it is only destroyed through  $\alpha$ -captures. In all cases Li is overproduced if we can assume that a sufficient supply of  $^3\text{He}$  is still available in the envelope when the VLTP begins (cf. Sect. 1.2).

Mg is more abundant in the simulations by one order of magnitude compared to observations. In all runs Mg is only weakly modified by nucleosynthesis. For this reason, the low observed Mg abundance may be another indicator of a sub-solar initial metallicity of the star, unless there is some observational problem.

Despite the differences between these tests and the measurements, the overall abundance trends are similar. In particular all three test cases in Fig 8 have a low [hs/ls] that ranges between -0.9 and -1.5, decreasing with increasing the split delay. In the case with the latest split (at 1200min), [hs/ls] is still  $\sim 0.5$ dex higher than observed in Sakurai's object. Light and intermediate elements are not much affected by the split time.

In addition to the split delay time the quantitative model predictions depend on the base stratification and convective mixing coefficient taken from the stellar evolution model. This determines, for instance, how quickly the protons and resulting  $^{13}\text{C}$  are mixed, and in turn the neutron density. To test the dependence of the results on this point we present another set of simulations based on the structure (strat-B) at the last thermal pulse in the  $2M_{\odot}$  star model sequence by Herwig et al. (model ET14 2006). We have applied a delayed split as for the strat-A model. With this base structure, the measured [hs/ls] is reproduced within the uncertainties (Fig. 9). However, now Zr is higher by 1 dex compared to the Asplund et al. measurements. A general overview of the abundance profiles in the He intershell for the most indicative light isotopes and of the elements included in Fig. 9 is given in Fig. 10, where the split position and the variation in the abundances are shown.

Fig. 10 (left upper panel) confirms that the  $^{12}\text{C}/^{13}\text{C} = 6.7$  ratio agrees within uncertainties with the observed ratio of  $\sim 3 \dots 5$ .  $^7\text{Be}$  is shown in the lower left panel to be highly abundant, which will feed Li.

This profile view of one of our simulations reveals that the neutron capture nucleosynthesis continues below the split, thereby further modifying chemical abundances. Possibly this further processed material below the split has affected Sakurai's observed surface abundances, through additional, later mixing. H-burning at the split must lose efficiency at some point when running out of fuel. This may allow material exchange between the two regions (see also discussion in Asplund et al. 1999). Asplund et al. observed Sakurai's object four different times in 6 months, and these observations show some drastic changes for some elements. It is not the aim of this paper to directly address these abundance trends over the sixth-month period, since this level of detail cannot be captured by our modeling approach, but has to await updated multi-dimensional simulations.

However, we may assume, as a working hypothesis, that the He intershell is made of two components, one heavily processed below the split (region 1), and one above the split (region 2) that was affected only by the first ingestion phase. Because of the decreasing of efficiency of the H-burning at the split, some material from region 1 is allowed to reach region 2 again and contribute to the observed abundance distribution. Such a two-component model is shown in Fig. 11. Starting from the simulation based on stratification strat-A, with a delayed split after

1200min (see Fig. 8) 10% of the material is coming from region 1, and 90% from region 2. No significant differences are obtained compared to Fig. 8. However, this depends on how much material is mixed from region 1 to region 2. In this specific case, such mixing implies a decrease on [hs/ls], but also an increase on Ba production, not supported from the observations. For this reason, at present we cannot confirm or rule out such a double component scenario.

#### 5.4. Nuclear reaction rate uncertainties

In this nucleosynthesis scenario both H- and He-burning reactions, as well as the n-capture reactions including those of short-lived isotopes, are important. Especially, several elemental abundances, for example Ti and Sc, are strongly dependent on s-process branchings which requires extra accuracy from the nuclear physics data. As we want to use this case to probe future hydrodynamic simulations we need to assess the influence of nuclear rate uncertainties.

In Fig. 12 we show for the model strat-A with split after 1000min the impact of changing the  $^{13}\text{C}(\alpha,n)^{16}\text{O}$  and the  $^{14}\text{N}(n,p)^{14}\text{C}$  reactions by a factor of 2. The  $^{25}\text{Mg}(n,\gamma)^{26}\text{Mg}$  reaction has been varied by a factor of 1.2.  $^{13}\text{C}(\alpha,n)^{16}\text{O}$  is the main neutron source and the two neutron capture reactions are important neutron poisons. Among these tests, the [hs/ls] changes between -0.9 and -1.6. In particular the first peak elements are strongly affected. The Rb abundance changes by 1dex. Intermediate and light element predictions are only weakly affected by nuclear reaction rate uncertainties. Small errors associated with the CNO cycle rates (e.g.,  $^{12}\text{C}(p,\gamma)^{13}\text{N}$  and  $^{14}\text{N}(p,\gamma)^{15}\text{O}$ ) have a marginal impact in our results compared to the other rates that we have considered.

In Fig. 12, we only included the impact of varying the neutron capture reaction rates of light neutron poisons. In the short time scale of the neutron burst, the neutron capture process is also expected to show a strong propagation effect in the final abundance distribution beyond iron, due to uncertainties of neutron capture rates along the nucleosynthesis path. In particular, such propagation may be relevant in our case, since Rb, Sr, Y and Zr production is affected by the error of several low cross sections of isotopes in the mass region between Fe and Sr, acting like bottle-necks in the neutron capture flow (e.g.,  $^{62}\text{Ni}$ ,  $^{68}\text{Zn}$ ,  $^{74}\text{Ge}$  and  $^{78}\text{Se}$  Pignatari et al. 2010, and reference therein). Another point to consider is that in the high neutron density regime reached in our calculations several unstable isotopes are produced efficiently, and many stable isotopes receive a significant contribution from unstable species from radiogenic decay and/or from decay during the neutron freezout, when the split is established. For instance, in all the cases presented in Fig. 12 most of Y (that is formed by one stable isotope only,  $^{89}\text{Y}$ ) is produced as  $^{89}\text{Sr}$ . The neutron capture rates of unstable species are mostly theoretical, and also their large uncertainty (typically a factor of 2-3) may affect the final isotopic distribution.

None of our simulations seem to be reproducing Sc particularly well. Sc and the elemental ratio Sc/Ca are particularly sensitive to the neutron density. Indeed,  $^{45}\text{Sc}$  is produced as unstable  $^{45}\text{Ca}$  via neutron captures on stable Ca species, where  $^{40}\text{Ca}$  is the main seed for Sc production.  $^{41}\text{Ca}$  is unstable, and has stronger (n,p) and (n, $\alpha$ ) than (n, $\gamma$ ) channels. For this reason, the uncertainty in the relative efficiency of the (n,p), (n, $\alpha$ ) and (n, $\gamma$ ) channels may affect the total Sc production. Among nuclear uncertainties, another possible explanation for Sc over-



production is that the initial metallicity of the Sakurai's object is even lower than what we have used for our simulations ( $[\text{Fe}/\text{H}]=-0.18$ ). Indeed, a lower initial  $^{40}\text{Ca}$  will result in a lower final Sc abundance.

## 6. CONCLUSIONS

### 6.1. Summary

We have presented in this paper a multi-physics view of the combustion in a very-late thermal pulse in a pre-WD. H is mixed convectively into the He-shell flash convection zone. We have discussed the one-dimensional stellar evolution picture, that predicts that early on the energy generation from the  $^{12}\text{C}(p,\gamma)^{13}\text{N}$  reaction creates a sharp entropy discontinuity which prohibits mixing. A detailed nucleosynthesis analysis, based on a complete multi-zone treatment of nucleosynthesis with mixing, shows that this one-dimensional structure evolution leads to abundance predictions that are incompatible with the observed abundances in Sakurai's object. Seeking guidance from full three-dimensional hydrodynamic simulations of He-shell flash convection in  $4\pi$  geometry with entrainment, we obtain reasons to suspect that the burning front is more distributed than predicted in one-dimensional stellar evolution. Fuel will be transported down in down-draft lanes leading to an inhomogeneous distribution of fuel in the burning zone. In addition, vertical down drafts enriched with fuel will populate a velocity distribution. From this information we speculate that mixing of protons and of the neutron source material  $^{13}\text{N}$  which later becomes  $^{13}\text{C}$ , across the convective H-burning zone will proceed for much longer than indicated by one-dimensional stellar evolution.

We point out that the main nucleosynthetic signature of convective-reactive burning in this study is the significant overproduction of the first peak elements Sr, Y and Zr, coupled with a non-efficient production of the second peak elements Ba and La. According to our simulations, neutron densities  $10^{12}\text{ cm}^{-3} < N_n < 10^{16}\text{ cm}^{-3}$  are required to explain such abundance distribution. More specifically, in the Sakurai's object time scale of  $\sim 2$  years between the luminosity peak due to H burning and the Asplund's observations, a neutron density peak of  $\sim 10^{15}\text{ cm}^{-3}$  with a delay of  $\sim 1$  day before the complete split activation would qualitatively reproduce the observed [hs/ls] ratio, the Li abundance and the low  $^{12}\text{C}/^{13}\text{C}$  ratio. The problems that we encounter in reproducing single elements may be due to the approximations in our model (e.g., for the nucleosynthesis simulations we use parameters from one-dimensional stellar models), to observation problems (e.g., the observed Y/Zr ratio cannot be reproduced by neutron capture nucleosynthesis) or to nuclear physics uncertainties (e.g., Sc).

Nuclear reaction rate uncertainties are shown to have a particularly important effect on some key observables in this non-

equilibrium nuclear burning environment.

### 6.2. Implications for stellar evolution and nucleosynthesis of the first generations of stars

One of our main motivations to study convective-reactive phases in stellar evolution is their prevalence in models of the first generation of stars. As reviewed in Sect. 1.1, convective mixing of protons with the  $^{12}\text{C}$  from He-burning at He-burning temperatures is frequently encountered in stellar evolution calculations at very low and zero metal content at all masses. This investigation shows that the predictive power of one-dimensional stellar evolution simulations is severely limited for observables that depend on these convective-reactive phases.

Neutron burst nucleosynthesis of the type described in this paper are nevertheless expected to happen also in the convective-reactive H- $^{12}\text{C}$  combustion events in first generation of stars. Indeed, the neutron source  $^{13}\text{C}$  is of primary origin, i.e. its abundance is not affected by the metal content in the initial stellar composition. Massive stars at different metallicities may experience H- $^{12}\text{C}$  combustion, ingesting protons in the He shell (see discussion in Woosley & Weaver 1995). If enough hydrogen fuel is ingested then Sr, Y and Zr may be efficiently produced by the primary  $^{13}\text{C}(\alpha,n)^{16}\text{O}$  neutron source, just as in our simulations presented here. This may be an alternative or complementary explanation for a missing component in the first neutron-peak region of the abundance distribution in both the solar abundance distribution as well as the metal poor stars, (light-element primary process, or LEPP Travaglio et al. 2004; Pignatari et al. 2008; Farouqi et al. 2009). In the future we intend to study the speculation that the convective-reactive proton- $^{12}\text{C}$  combustion in the convective He shell in massive stars could provide another possible solution for the LEPP.

FH acknowledges NSERC Discovery Grant funding. The hydrodynamics simulations were performed by PRW on a cluster of workstations at the University of Minnesota, provided through an NSF equipment grant, NSF-CNS-0708822. The work of CF and GR was funded in part under the auspices of the National Nuclear Security Administration of the U.S. Department of Energy at Los Alamos National Laboratory and supported by Contract No. DE-AC52-06NA25396. RH acknowledges support from the World Premier International Research Center Initiative (WPI Initiative), MEXT, Japan. This work used the SE library (LA-CC-08-057) developed at Los Alamos National Laboratory as part of the NuGrid collaboration; SE makes use of the HDF5 library, which was developed by The HDF Group and by the National Center for Supercomputing Applications at the University of Illinois at Urbana-Champaign.

## REFERENCES

- Abia, C. & Wallerstein, G. 1998, *MNRAS*, 293, 89  
 Angulo, C., Arnould, M., & Rayet, M. et al. 1999, *Nucl. Phys.*, A 656, 3, NACRE compilation  
 Aoki, W., Norris, J. E., Ryan, S. G., Beers, T. C., & Ando, H. 2000, *ApJ*, 536, L97  
 Arnett, D. 1996, *Supernovae and Nucleosynthesis: An Investigation of the History of Matter, from the Big Bang to the Present* (Princeton University Press)  
 Asplund, M., Grevesse, N., & Sauval, A. J. 2005, in *Astronomical Society of the Pacific Conference Series*, Vol. 336, *Cosmic Abundances as Records of Stellar Evolution and Nucleosynthesis*, ed. T. G. Barnes, III & F. N. Bash, 25–+
- Asplund, M., Grevesse, N., Sauval, A. J., & Scott, P. 2009, *ARA&A*, 47, 481  
 Asplund, M., Lambert, D. L., Kipper, T., Pollacco, D., & Shetrone, M. D. 1999, *A&A*, 343, 507  
 Beveridge, R. C. & Sneden, C. 1994, *AJ*, 108, 285  
 Blöcker, T. 1995, *A&A*, 297, 727  
 Blondin, J. M. & Lufkin, E. A. 1993, *APJS*, 88, 589  
 Brown, T. M., Sweigart, A. V., Lanz, T., Landsman, W. B., & Hubeny, I. 2001, *ApJ*, 562, 368  
 Bryan, G. L., Norman, M. L., Stone, J. M., Cen, R., & Ostriker, J. P. 1995, *Computer Physics Communications*, 89, 149  
 Burbidge, E. M., Burbidge, G. R., Fowler, W. A., & Hoyle, F. 1957, *Rev. Mod. Phys.*, 29, 547

- Busso, M., Gallino, R., Lambert, D. L., Travaglio, C., & Smith, V. V. 2001, *ApJ*, 557, 802
- Calder, A. C., Fryxell, B., Plewa, T., Rosner, R., Dursi, L. J., Weirs, V. G., Dupont, T., Robey, H. F., Kane, J. O., Remington, B. A., Drake, R. P., Dimonte, G., Zingale, M., Timmes, F. X., Olson, K., Ricker, P., MacNeice, P., & Tufo, H. M. 2002, *ApJS*, 143, 201
- Campbell, S. W. & Lattanzio, J. C. 2008, *A&A*, 490, 769
- Cassisi, S., Iben, I. J., & Tornambe, A. 1998, *ApJ*, 496, 376
- Chapman, S. 1961, *Proc. Phys. Soc.*, 77, 424
- Charbonnel, C. & Zahn, J. 2007, *A&A*, 467, L15
- Colella, P. & Woodward, P. R. 1984, *Journal of Computational Physics*, 54, 174
- Crastello, S., Piersanti, L., Straniero, O., Gallino, R., Domínguez, I., & Käppeler, F. 2009, *Publications of the Astronomical Society of Australia*, 26, 139
- Denissenkov, P. A. 2010, *ApJ* 723, 563.
- Dillmann, I., Heil, M., Käppeler, F., Plag, R., Rauscher, T., & Thielemann, F.-K. 2006, in *American Institute of Physics Conference Series*, Vol. 819, *Capture Gamma-Ray Spectroscopy and Related Topics*, ed. A. Woehr & A. Arahamian, 123–127
- Dimotakis, P. E. 2005, *Annu. Rev. Fluid Mech.*, 37, 329
- Duerbeck, H. W., Liller, W., Sterken, C., Benetti, S., van Genderen, A. M., Arts, J., Kurk, J. D., Janson, M., Voskes, T., Brogt, E., Arentoft, T., van der Meer, A., & Dijkstra, R. 2000, *AJ*, 119, 2360
- Ekström, S., Meynet, G., Chiappini, C., Hirschi, R., & Maeder, A. 2008, *A&A*, 489, 685
- Farouqi, K., Kratz, K., Mashonkina, L. I., Pfeiffer, B., Cowan, J. J., Thielemann, F., & Truran, J. W. 2009, *ApJ*, 694, L49
- Fujimoto, M. Y., Ikeda, Y., & Iben, I. J. 2000, *ApJ Lett.*, 529, L25
- Fuller, G. M., Fowler, W. A., & Newman, M. J. 1985, *ApJ*, 293, 1
- Fynbo, H. O. U., Diget, C. A., Bergmann, U. C., Borge, M. J. G., Cederkäll, J., Dendooven, P., Fraile, L. M., Franchoo, S., Fedosseev, V. N., Fulton, B. R., Huang, W., Huikari, J., Jeppesen, H. B., Jokinen, A. S., Jones, P., Jonson, B., Köster, U., Langanke, K., Meister, M., Nilsson, T., Nyman, G., Prezado, Y., Riisager, K., Rinta-Antila, S., Tengblad, O., Turrión, M., Wang, Y., Weissman, L., Wilhelmsen, K., Äystö, J., & The ISOLDE Collaboration, a. 2005, *Nature*, 433, 136
- Goriely, S. 1999, *A&A*, 342, 881
- Goriely, S. & Siess, L. 2004, *A&A*, 421, L25
- Heil, M., Detwiler, R., Azuma, R. E., Couture, A., Daly, J., Görres, J., Käppeler, F., Reifarth, R., Tischhauser, P., Ugalde, C., & Wiescher, M. 2008, *Phys. Rev. C*, 78, 025803
- Herwig, F. 2000, *A&A*, 360, 952
- , 2001, *ApJ Lett.*, 554, L71
- , 2004, *ApJ*, 605, 425
- Herwig, F. & Austin, S. M. 2004, *ApJ Lett.*, 613, L73
- Herwig, F., Austin, S. M., & Lattanzio, J. C. 2006, *Phys. Rev. C*, 73, 025802
- Herwig, F., Bennett, M., Diehl, S., Fryer, C. L., Hirschi, R., Hungerford, A., Magkotsios, G., Pignatari, M., Rockefeller, G., Timmes, F. X., & Young, P. 2008, *PoSArXiv e-prints*, NIC X
- Herwig, F., Blöcker, T., Langer, N., & Driebe, T. 1999, *A&A*, 349, L5
- Herwig, F., Freytag, B., Hueckstaedt, R. M., & Timmes, F. X. 2006, *ApJ*, 642, 1057
- Herwig, F. & Langer, N. 2001, *Nuclear Physics A*, 688, 221
- Hollowell, D., Iben, I. J., & Fujimoto, M. Y. 1990, *ApJ*, 351, 245
- Iben, Jr., I., Kaler, J. B., Truran, J. W., & Renzini, A. 1983, *ApJ*, 264, 605
- Imbriani, G., Costantini, H., Formicola, A., Vomiero, A., Angulo, C., Bemmerer, D., Bonetti, R., Brogini, C., Confortola, F., Corvisiero, P., Cruz, J., Descouvemont, P., Fülöp, Z., Gervino, G., Guglielmetti, A., Gustavino, C., Gyürky, G., Jesus, A. P., Junker, M., Klug, J. N., Lemut, A., Menegazzo, R., Prati, P., Roca, V., Rolfs, C., Romano, M., Rossi-Alvarez, C., Schümann, F., Schürmann, D., Somorjai, E., Straniero, O., Strieder, F., Terrasi, F., & Trautvetter, H. P. 2005, *European Physical Journal A*, 25, 455
- Iwamoto, N., Kajino, T., Mathews, G. J., Fujimoto, M. Y., & Aoki, W. 2004, *ApJ*, 602, 378
- Kipper, T. & Jørgensen, U. G. 1994, *A&A*, 290, 148
- Kipper, T., Jørgensen, U. G., Klochkova, V. G., & Panchuk, V. E. 1996, *A&A*, 306, 489
- Kovacs, N. 1985, *A&A*, 150, 232
- Kunz, R., Fey, M., Jaeger, M., Mayer, A., Hammer, J. W., Staudt, G., Harissopoulos, S., & Paradellis, T. 2002, *ApJ*, 567, 643
- Lawlor, T. M. & MacDonald, J. 2003, *ApJ*, 583, 913
- Lodders, K. 2003, *ApJ*, submitted
- Lodders, K., Palme, H., & Gail, H. 2009, *ArXiv e-prints*
- Luck, R. E. & Bond, H. E. 1991, *ApJS*, 77, 515
- McWilliam, A. 1998, *AJ*, 115, 1640
- McWilliam, A., Preston, G. W., Sneden, C., & Searle, L. 1995, *AJ*, 109, 2757
- Miller Bertolami, M. M. & Althaus, L. G. 2007, *MNRAS*, 380, 763
- Miller Bertolami, M. M., Althaus, L. G., Serenelli, A. M., & Panei, J. A. 2006, *A&A*, 449, 313
- Miller Bertolami, M. M., Althaus, L. G., Unglaub, K., & Weiss, A. 2008, *A&A*, 491, 253
- Norris, J. E., Ryan, S. G., & Beers, T. C. 1997, *ApJ*, 489, L169+
- Oda, T., Hino, M., Muto, K., Takahara, M., & Sato, K. 1994, *Atomic Data and Nuclear Data Tables*, 56, 231
- Pereira, C. B., Smith, V. V., & Cunha, K. 1998, *AJ*, 116, 1977
- Pignatari, M., Gallino, R., Heil, M., Wiescher, M., Käppeler, F., Herwig, F., & Bisterzo, S. 2010, *ApJ*, 710, 1557
- Pignatari, M., Gallino, R., Meynet, G., Hirschi, R., Herwig, F., & Wiescher, M. 2008, *ApJ Lett.*
- Piro, A. L. & Bildsten, L. 2007, *ApJ*, 663, 1252
- Porter, D. H. & Woodward, P. R. 2006, in *Implicit Large Eddy Simulation: Computing Turbulent Fluid Dynamics*, ed. L. M. F. Grinstein & W. Rider, Cambridge University Press, <http://www.lcse.umn.edu/ILES>
- Porter, D. H., Woodward, P. R., & Jacobs, M. L. 2000, in *New York Academy Sciences Annals*, Vol. 898, *Astrophysical Turbulence and Convection*, ed. J. R. Buchler & H. Kandrump, 1–4, online at <http://www.lcse.umn.edu/convspsh>
- Reddy, B. E., Bakker, E. J., & Hrivnak, B. J. 1999, *ApJ*, 524, 831
- Reifarth, R., Käppeler, F., Voss, F., Wisshak, K., Gallino, R., Pignatari, M., & Straniero, O. 2004, *ApJ*, 614, 363
- Scalo, J. M., Despain, K. H., & Ulrich, R. K. 1975, *ApJ*, 196, 805
- Schlattl, H., Salaris, M., Cassisi, S., & Weiss, A. 2002, *A&A*, 395, 77
- Smith, V. V. 1984, *A&A*, 132, 326
- Smith, V. V., Coleman, H., & Lambert, D. L. 1993, *ApJ*, 417, 287
- Smith, V. V., Cunha, K., Jorissen, A., & Boffin, H. M. J. 1996, *A&A*, 315, 179
- , 1997, *A&A*, 324, 97
- Smith, V. V. & Lambert, D. L. 1984, *PASP*, 96, 226
- , 1985, *ApJ*, 294, 326
- , 1986, *ApJ*, 311, 843
- Smith, V. V. & Lambert, D. L. 1990, *ApJS*, 72, 387
- Smith, V. V. & Suntzeff, N. B. 1987, *AJ*, 93, 359
- Suda, T., Aikawa, M., Machida, M. N., Fujimoto, M. Y., & Iben, I. J. 2004, *ApJ*, 611, 476
- Tech, J. L. 1971, A high dispersion spectral analysis of the Ba\_II star HD 204075 (zeta\_Capricorni). (*Natl. Bureau Standards*, Washington, D.C., NBS Monograph 11)
- Tomkin, J. & Lambert, D. L. 1983, *ApJ*, 273, 722
- , 1986, *ApJ*, 311, 819
- Travaglio, C., Gallino, R., Arnone, E., Cowan, J., Jordan, F., & Sneden, C. 2004, *ApJ*, 601, 864
- van Hoof, P. A. M., Hajduk, M., Zijlstra, A. A., Herwig, F., Evans, A., van de Steene, G. C., Kimeswenger, S., Kerber, F., & Eyres, S. P. S. 2007, *A&A*, 471, L9
- van Leer, B. 1977, *Journal of Computational Physics*, 23, 276
- Van Winckel, H. & Reyniers, M. 2000, *A&A*, 354, 135
- Vanture, A. D. 1992, *AJ*, 104, 1986
- Vanture, A. D. 2000, private communication
- Wallerstein, G., Iben, Jr., I., Parker, P., Boesgard, A. M., Hale, G. M., Champagne, A. E., Barnes, C. A., Käppeler, F., Smith, V. V., Hoffmann, R. D., Timmes, F. X., Sneden, C., Boyd, R. N., Meyer, B. S., & Lambert, D. L. 1997, *Rev. Mod. Phys.*, 69, 995
- Wasserburg, G. J., Boothroyd, A. I., & Sackmann, I.-J. 1995, *ApJ Lett.*, 447, L37
- Woodward, P. & Colella, P. 1984, *Journal of Computational Physics*, 54, 115
- Woodward, P., Herwig, F., Porter, D., Fuchs, T., Nowatzki, A., & Pignatari, M. 2008, in *American Institute of Physics Conference Series*, Vol. 990, *First Stars III*, 300–308
- Woodward, P. R. 1986, in *Astrophysical Radiation Hydrodynamics*, ed. K.-H. Winkler & M. L. Norman, Reidel, 245–326, online at [http://www.lcse.umn.edu/projects/34/34\\_PPMlogoPaper.pdf](http://www.lcse.umn.edu/projects/34/34_PPMlogoPaper.pdf)
- Woodward, P. R. 2005, *PPB: the Piecewise-Parabolic Boltzmann Scheme for Moment-Conserving Advection in 2 and 3 Dimensions*, LCSE internal report, University of Minnesota, available at <http://www.lcse.umn.edu/PPBdocs>
- Woodward, P. R. 2006, in *Implicit Large Eddy Simulation, Computing Turbulent Fluid Dynamics*, ed. L. M. F. Grinstein & W. Rider, Cambridge University Press, available at <http://www.lcse.umn.edu/ILES/PPM-for-ILES-turb-apps-2-26-05-cup6a-10.pdf>
- Woodward, P. R., Jayaraj, J., Lin, P.-H., & Dai, W. 2009, in *Concurrency and Computation Practice and Experience*, in press, available at <http://www.lcse.umn.edu/RR-experience>
- Woodward, P. R., Jayaraj, J., Lin, P.-H., & Yew, P.-C. 2008, in *Computing in Science & Engineering*, in press, online at <http://www.lcse.umn.edu/ILES/PPM-for-ILES-turb-apps-2-26-05-cup6a-10.pdf>
- Woodward, P. R., Porter, D. H., Anderson, S., Fuchs, T., & Herwig, F. 2006, *Journal of Physics Conference Series*, 46, 370
- Woodward, P. R., Porter, D. H., Herwig, F., Pignatari, M., Jayaraj, J., & Lin, P. 2008, in *Nuclei in the Cosmos (NIC X)*
- Woodward, P. R., Porter, D. H., & Jacobs, M. 2003, in *Astronomical Society of the Pacific Conference Series*, Vol. 293, *3D Stellar Evolution*, ed. S. Turcotte, S. C. Keller, & R. M. Cavallo, 45–+, online at <http://www.lcse.umn.edu/3Dstars>
- Woolsey, S. E., Heger, A., Cumming, A., Hoffman, R. D., Pruet, J., Rauscher, T., Fisker, J. L., Schatz, H., Brown, B. A., & Wiescher, M. 2004, *ApJS*, 151, 75
- Woolsey, S. E. & Weaver, T. A. 1995, *ApJS*, 101, 181+
- Zacs, L., Klochkova, V. G., & Panchuk, V. E. 1995, *MNRAS*, 275, 764
- Zacs, L., Nissen, P. E., & Schuster, W. J. 1998, *A&A*, 337, 216
- Začs, L., Schmidt, M. R., & Schuster, W. J. 2000, *A&A*, 358, 1022

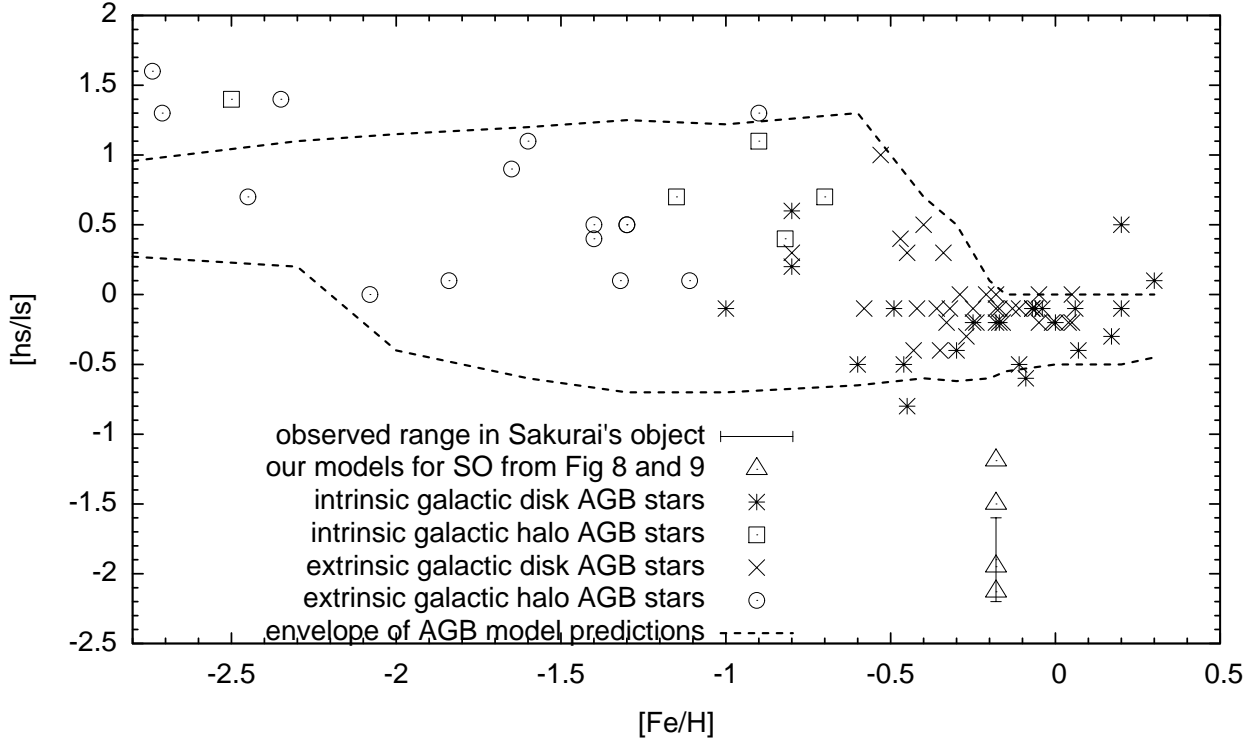


FIG. 1.— Observed and predicted  $s$ -process abundance distribution index ratio  $[hs/ls]$  for stars with a large range of metallicities. Observations (Tech 1971; Smith 1984; Smith & Lambert 1984, 1985, 1986; Smith & Suntzeff 1987; Smith & Lambert 1990; Smith et al. 1993, 1996, 1997; Abia & Wallerstein 1998; Van Winckel & Reyniers 2000; Zacs et al. 1995, 1998; Začs et al. 2000; Reddy et al. 1999; Kipper et al. 1996; Kipper & Jorgensen 1994; Tomkin & Lambert 1983, 1986; Kovacs 1985; Vanture 1992, 2000; Pereira et al. 1998; Aoki et al. 2000; McWilliam et al. 1995; McWilliam 1998; Norris et al. 1997; Beveridge & Sneden 1994) and model predictions of AGB stars are from Busso et al. (2001). In the Figure, the  $[hs/ls]$  ratio observations of the Sakurai's object have a certain range, depending on which of the 4 observations from Asplund et al. are considered, and how the indices are calculated. In general, the ratio is about 2dex smaller compared to AGB predictions and observations. Our nucleosynthesis results are also included for comparison (see Sect. 5 for details).

TABLE 1  
OBSERVED NEUTRON CAPTURE SIGNATURE, ASPLUND ET AL. (1999).

$[Fe/H] = 0 (-0.63)$	April 1996	October 1996
$[Y/Fe]$	+0.96 (+1.59)	+1.96 (+2.59)
$[Ba/Fe]$	-0.63 (0.0)	-0.23 (+0.40)
$[Ba/Y]$	-1.59 (-1.59)	-2.19 (-2.19)

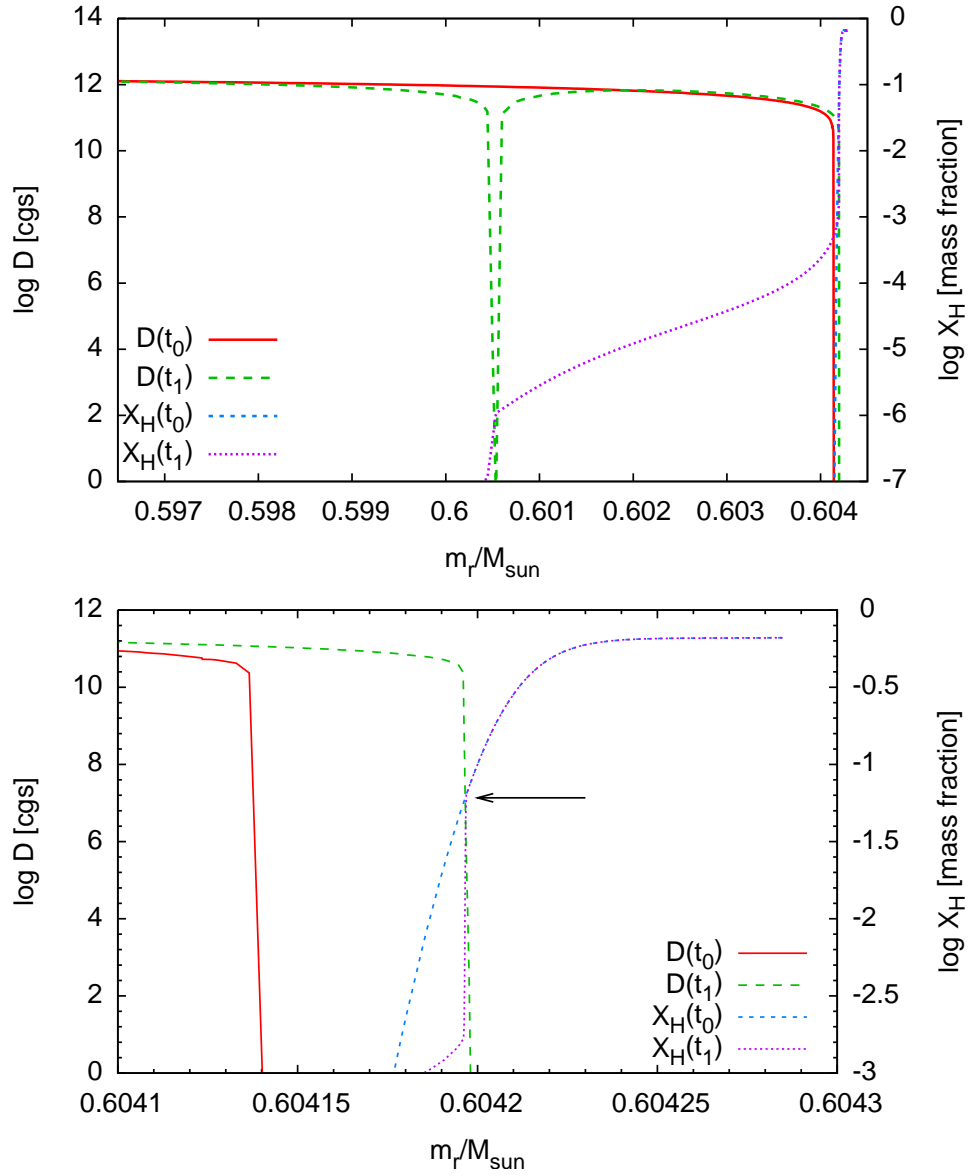


FIG. 2.— Convective diffusion coefficient and H abundance profile at the beginning of the H-ingestion flash  $t_0$  and at the time when the split of the convection zone appears at  $t_1 = t_0 + 8.58 \cdot 10^5$  s. Top panel: the outer section of the convection zone showing the location of the split as a deep dip in  $D$ ; bottom panel: just the interface of the outer boundary of the convection zone. The arrow indicates the H abundance at the position that has been reached by the convection zone at the time  $t_1$ .  $t_0$  is at the time of the minimum of the H-burning luminosity at the onset of the H-ingestion event.

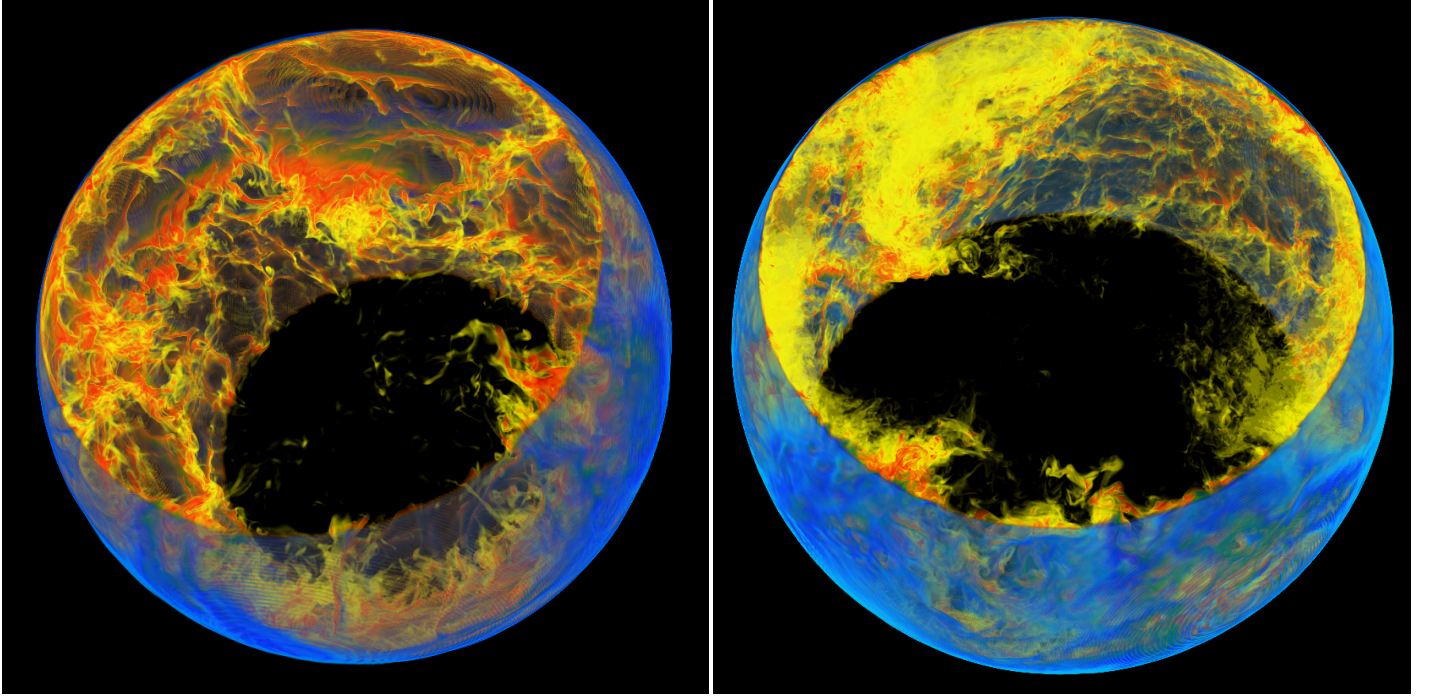


FIG. 3.— Hydrodynamic picture of H-entrainment into He-shell flash convection near the luminosity peak of the flash. The setup is based on a stellar evolution model corresponding to the situation shortly after time  $t_0$  shown in Fig. 2, when the top of the convection zone is just making contact with the H-rich stable layer. Colors indicate abundance of proton-rich material that is originally only in the stable layer above the convection zone that is entrained into the convection zone. Volume fractions of about  $\sim 1\%$  are shown as blue, while concentrations that are close to one are transparent. The lowest concentration yellow blobs that are mixed deep into the convection zone correspond to  $\sim 0.01\%$ . Abundance levels below approximately  $5 \times 10^{-5}$  have been made transparent as well. The left panel shows a snapshot from a  $384^3$  grid while the right panel image is from a run on a  $576^3$  grid. Slightly different times are shown and similar but not identical color maps have been used. The PPM simulation is described in more detail in Sect. 4.1, and the simulation code is described in Sect. A.2.

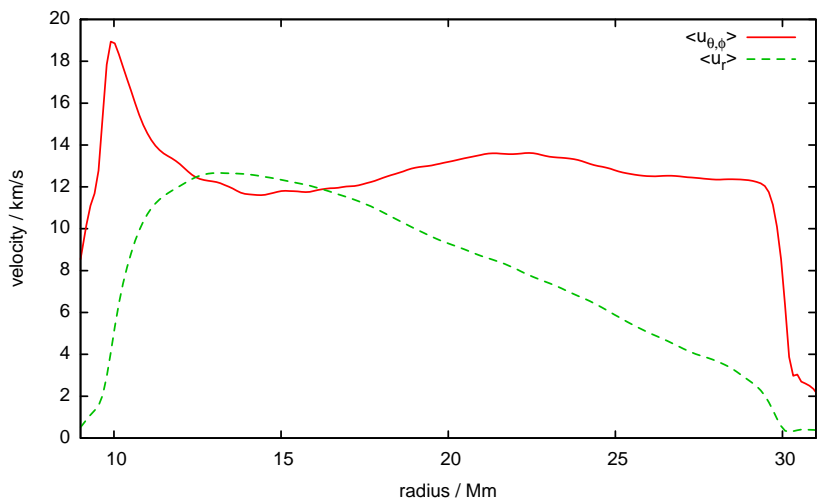


FIG. 4.— Radial and tangential radially averaged rms-velocities of the  $576^3$  simulation at the same time as shown (in the right panel) of Fig. 3.

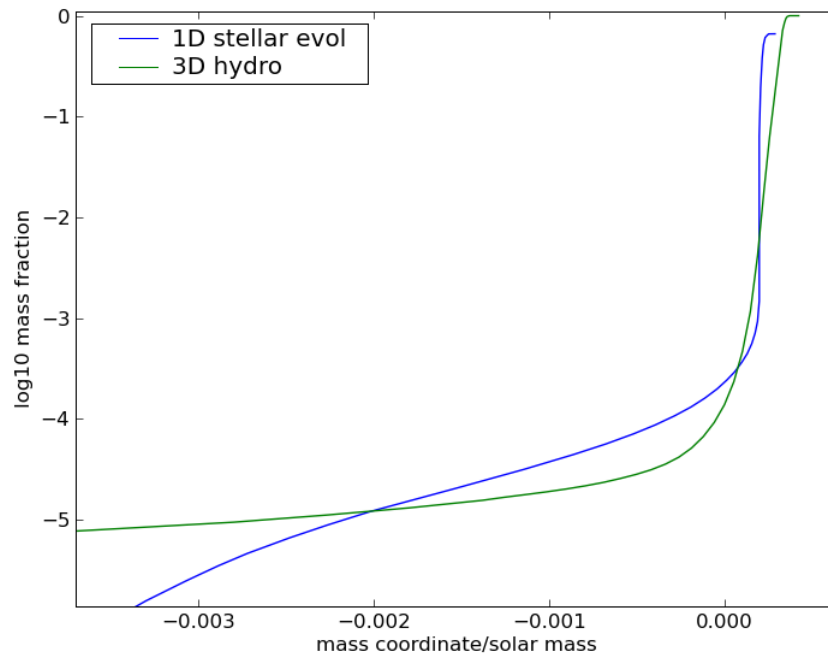


FIG. 5.— Comparison of entrainment of material from the stable layer above the convection zone into the  $^{12}\text{C}$ -rich layer as it is represented in the one-dimensional stellar evolution model with mixing treated as diffusion in the mixing-length picture and in the 3D simulations discussed in this paper. The 3D profile (green line) shows the same data, radially averaged, as in Fig. 3, right panel. The 1D line (blue) is the line labeled  $t_0$  in Fig. 2. The mass coordinates have been set to zero in both cases near the top of the convection zone.

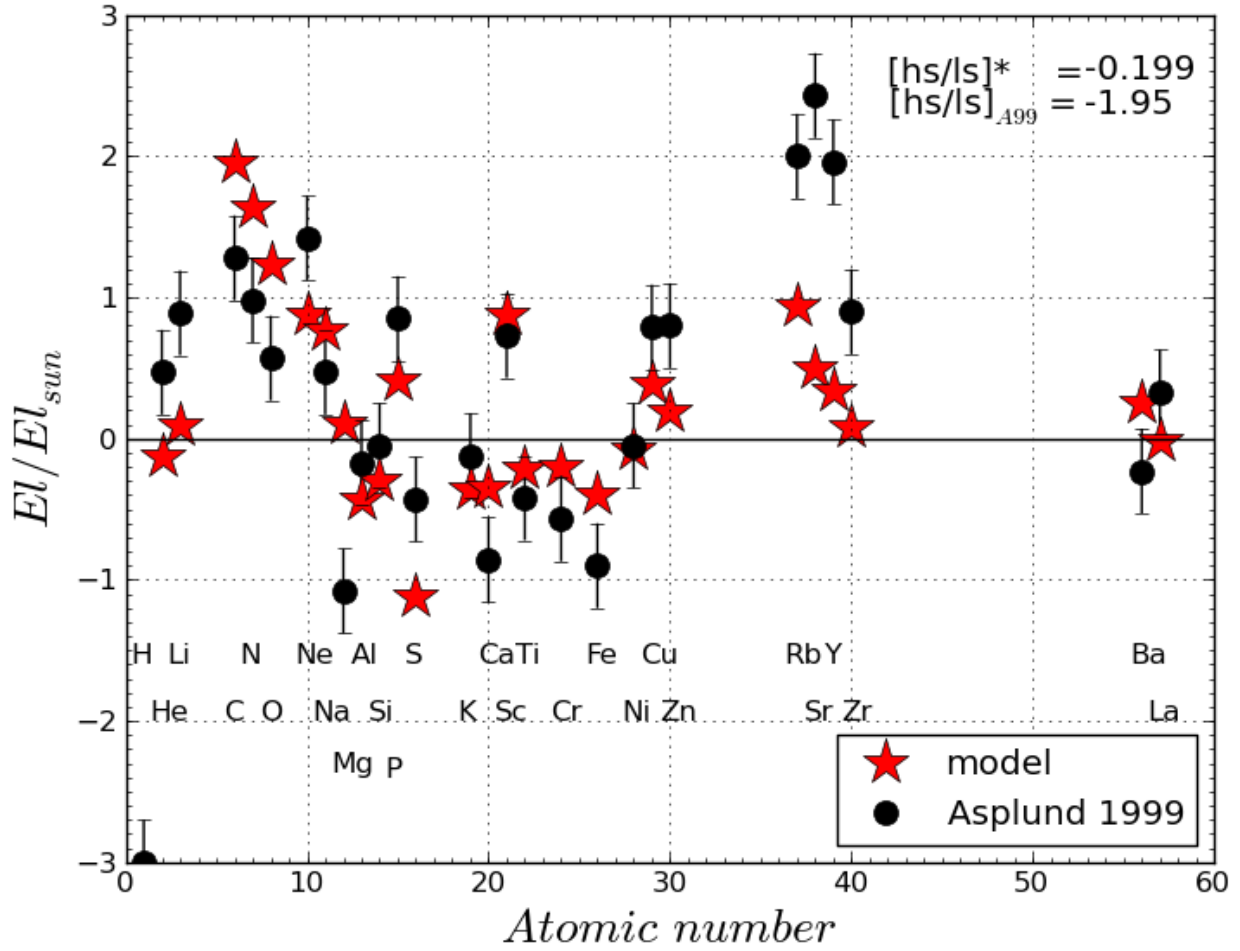


FIG. 6.— Abundance distribution obtained at the top of the He intershell assuming that the mixing split develops as soon as H is ingested. This case corresponds to the one-dimensional stellar evolution prediction for mixing in the H-ingestion flash. The abundances measured by Asplund et al. (1999) are reported for comparison.

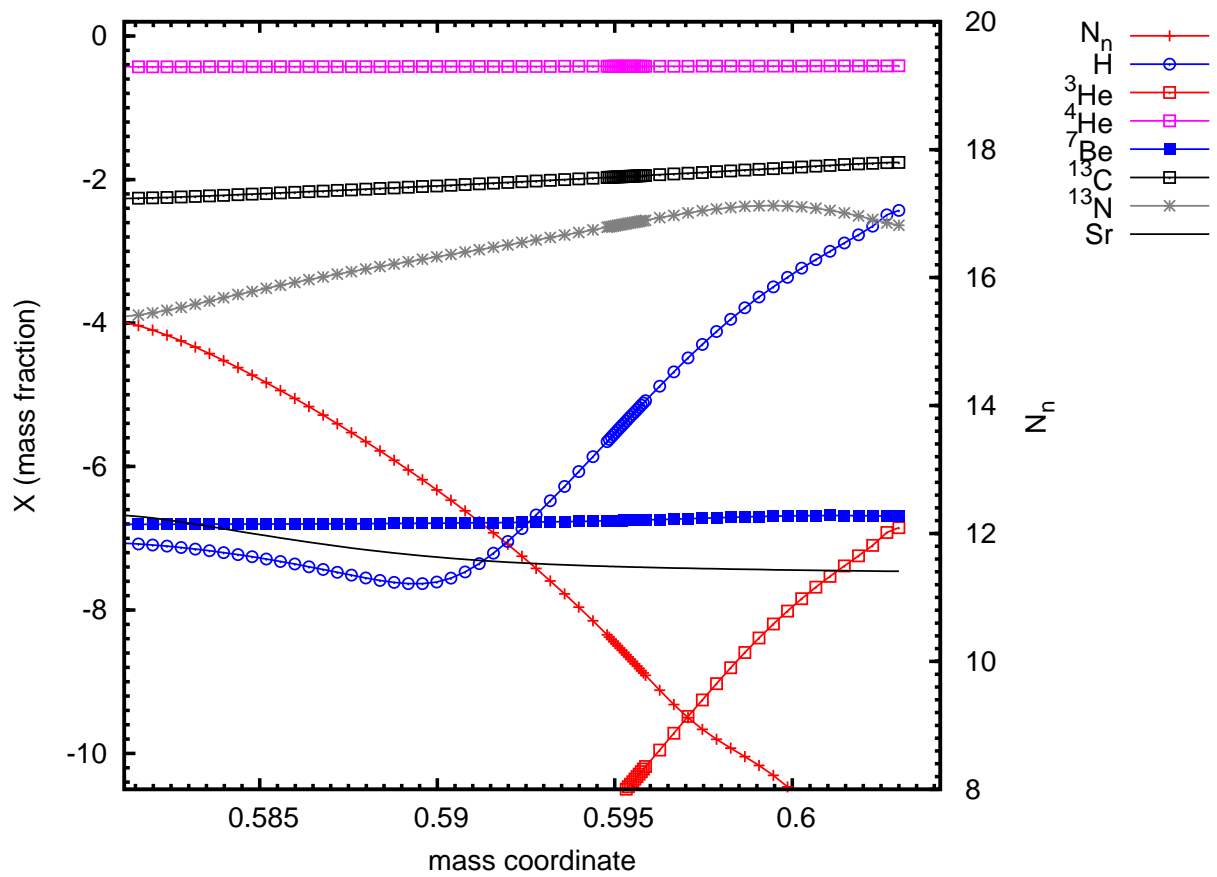


FIG. 7.— The abundance profiles snapshot (RUN103), just before the mixing split is imposed, demonstrates the simultaneous action of nucleosynthesis and mixing on similar time scales.



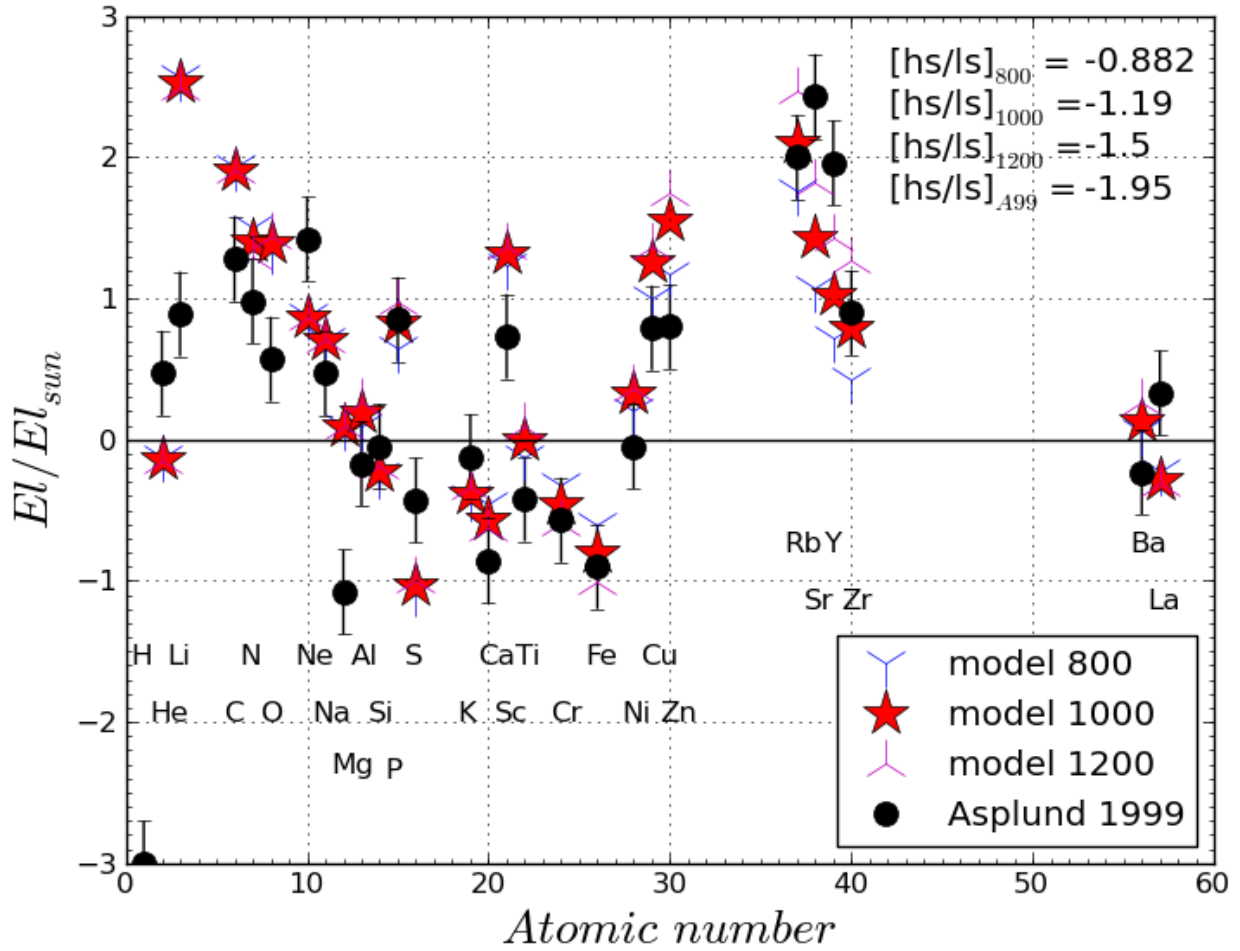


FIG. 8.— Abundance distribution at step 2000 for different cases with the split starting after 800min (RUN105), 1000min (RUN103) and 1200min (RUN106).

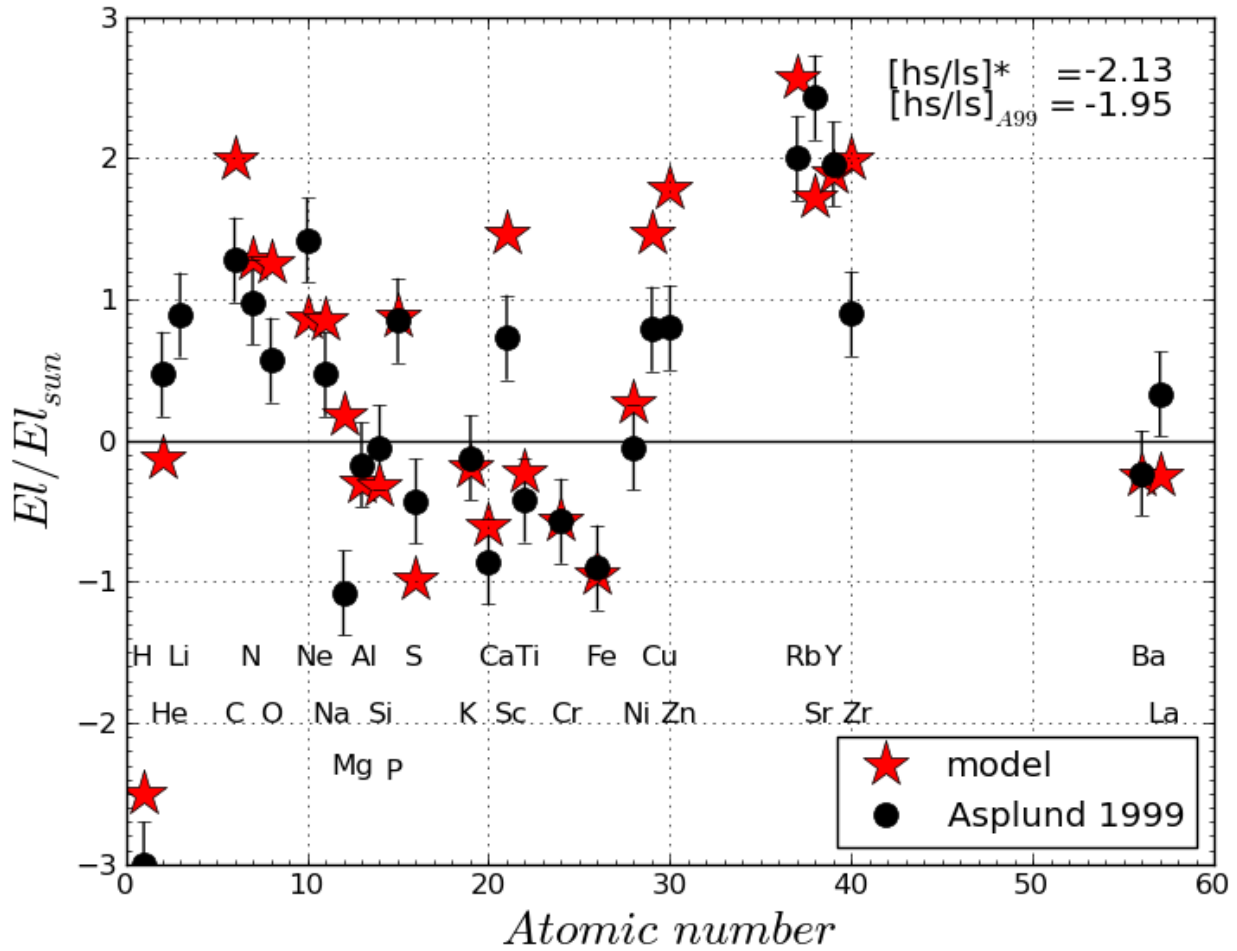


FIG. 9.— Abundance distribution at the end of the simulations (RUN48/strat-B) after 3000min, when all H- and  $^3\text{He}$ -ingestion has been ingested.

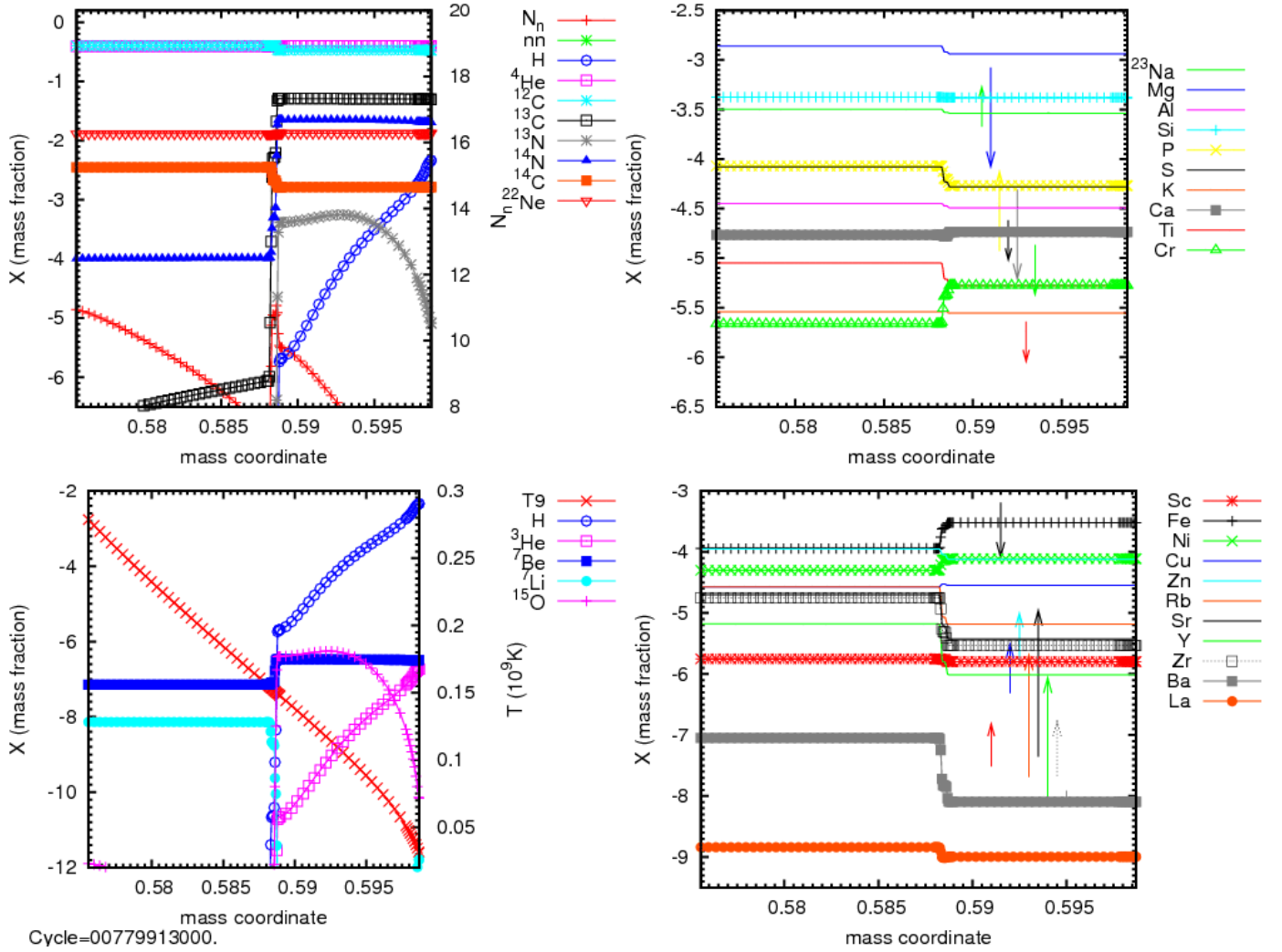


FIG. 10.— Abundance profile at the end of simulation RUN48 after 3000min, when all H- and  $^3\text{He}$  has been ingested. A split imposed at 950min has prevented further mixing between the He-shell flash driven convection zone (left) and the H-ingestion flash driven convection zone (right). Arrows in the right panels indicate the observed abundances, connecting the solar values with the observed ones.

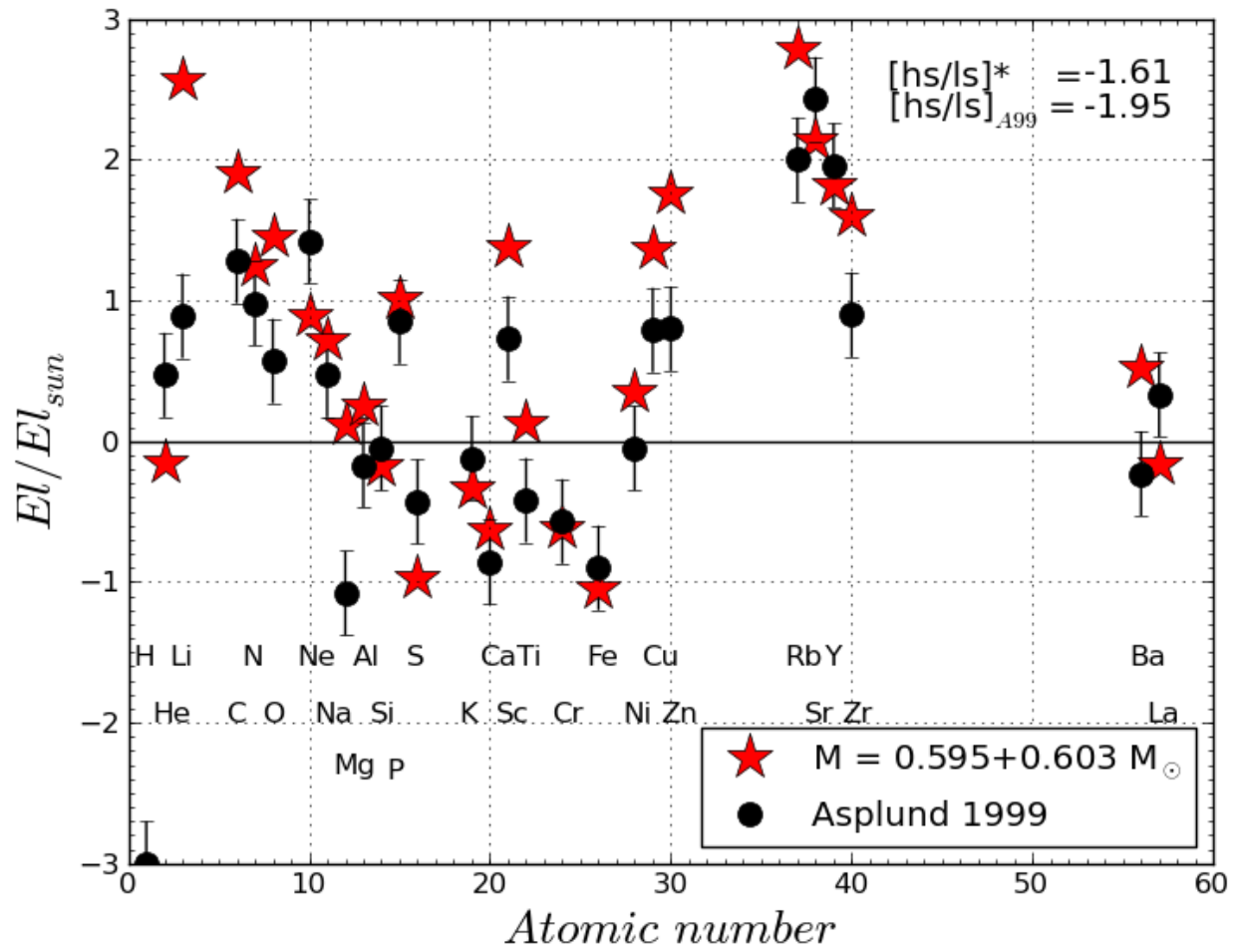


FIG. 11.— Abundance distribution at step 2000 for a split delay of 1200min, considering mixing of 10% of the deep component with 90% from the component above the split.

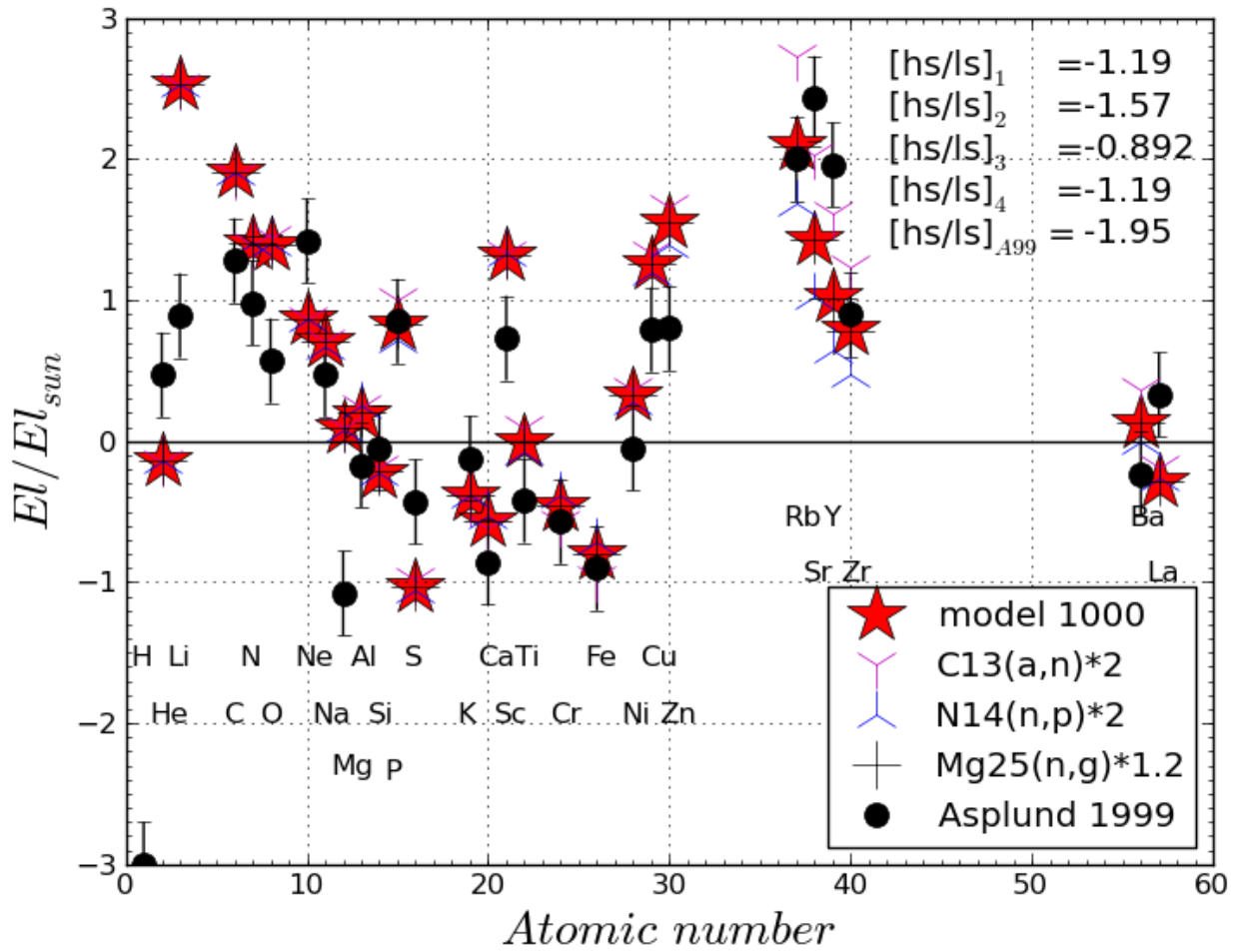


FIG. 12.— Abundance distribution for different nuclear test at step 2000, from RUN103 (split delay = 1000min) as standard, and RUN107,RUN108,RUN109.

## APPENDIX

## CODE DESCRIPTION

*Nucleosynthesis*

The PPN physics package allows a flexible combination of nuclear reaction rates and entire compilations of rates. For this study we choose for the main charged particle reactions the compilation by Angulo et al. (1999) (NACRE compilation). This choice allows us to be consistent with the original network used to calculate the stellar structures for basic energetic nuclear reactions, i.e.,  $^{14}\text{N}(p,\gamma)^{15}\text{O}$ ,  $3-\alpha$  and  $^{12}\text{C}(\alpha,\gamma)^{16}\text{O}$ . Notice that the use of more recent rates (e.g., Imbriani et al. 2005; Fynbo et al. 2005; Kunz et al. 2002, respectively) would not change our results, where uncertainties related to physics processes and mixing still has a critical impact. Other charged particle reactions, among the others  $^{13}\text{C}(\alpha,n)^{16}\text{O}$ , which is the main neutron source during the H ingestion, have more recent measurements (e.g., Heil et al. 2008). However, in this case NACRE rates are consistent with the new rates within their uncertainty. For instance, we consider a factor of two of uncertainty for the  $^{13}\text{C}(\alpha,n)^{16}\text{O}$  rate in the temperature regime that is relevant for the  $^{13}\text{C}$  burning (see Section 5 for more details). For neutron capture reactions of stable isotopes we refer to Dillmann et al. (2006) (KADoNIS compilation). Stellar  $\beta$ -decay rates and electron captures are from Oda et al. (1994) and Fuller et al. (1985) for many light unstable isotopes, and Goriely (1999) for many heavy unstable isotopes. Rates not included in the previous references are given by the Basel REACLIB compilation. We are solving the complete network in each radial grid point, including all relevant charged particle, n-capture reactions as well as the  $\beta$ -decays. A recursive, dynamic network generation has been integrated into the solver, i.e. the size of the network automatically adapts to the conditions given. If, for example, a neutron source is activated the network will be automatically enlarged to include all heavy and unstable isotopes as needed according to the network fluxes. This dynamic network feature ensures that the network calculation never misses any important isotope or reaction.

In these simulations we are using the multi-zone driver of the PPN code (MPPNP) that allows for the calculation of the complete nucleosynthesis in all of the zones of one-dimensional profiles, e.g. from stellar evolution, of density and temperature. The MPPNP driver employs MPI parallelism to enable efficient calculations on up to 30-50 processors depending on problem sizes. The simulations carried out here involve relatively small grids between 70 and 90 zones. A fully implicit nucleosynthesis step is followed by a mixing step according to the diffusion coefficient taken, for example, from the stellar evolution model. This procedure is repeated for subsequent time steps in order to compute the evolution of the abundance profiles of all species involved. Mixing and network calculations are performed in the operator split mode, which is a good approximation for the post-processing because we choose the post-processing time step to be small enough to resolve the mixing time scale.

*Hydrodynamics*

The PPM gas dynamics scheme (Woodward & Colella 1984; Colella & Woodward 1984; Woodward 1986, 2006) has been in use in computational astrophysics for many years. It is incorporated in the community codes VH1 (Blondin & Lufkin 1993), ENZO (Bryan et al. 1995), and FLASH (Calder et al. 2002). The version that we use in this work is described in full in Woodward (2006). Here we have augmented PPM with the PPB moment-conserving advection scheme to treat the entrainment of fluid from above the convection zone during the helium shell flash in an AGB star (see Woodward et al. 2008). PPB is built upon van Leer's Scheme VI (van Leer 1977), a 1-D scheme that conserves the first 3 moments of the advected distribution in each grid cell. To this scheme we have added a set of very carefully constructed constraints (Woodward 2005) keeping the advected fractional volume of a multifluid constituent of the gas within the range from 0 to 1. These constraints are a considerable improvement over those outlined in Woodward 1986 for a 2-D PPB scheme. We have also streamlined the implementation of PPB in 3-D by eliminating various high-order terms in order to obtain a highly efficient, directionally split scheme (Woodward 2005) that conserves 10 moments of the distribution of the advected fractional volume variable in each cell. PPB is combined with PPM to describe multifluid hydrodynamics by adding the constraint of pressure and temperature equilibrium within each grid cell. At present our code is explicit. Mach numbers in the convective gusts of helium shell flash convection are about 1/30 or less. Consequently, we must take many time steps to follow the flow through an entire circuit of a large convective eddy. We note that such eddies are global in scale, and we follow them by including the entire convection shell in our computational domain. The conclusion that large scales are involved here is similar to the earlier findings of Porter et al. (2000) and Porter & Woodward (2006) for the outer convective envelope of an AGB star. The restricted time step values, from explicit hydrodynamics, and the large domain, arising from the natural scale of the convection, place significant demands on the computation. We address these demands in two ways. First, we exploit a new implementation of our codes aimed specifically at the multicore CPUs found in modern computers (see Woodward et al. 2008, 2009), which has delivered to our codes roughly a 40x speed-up over performance on single-core platforms from about 4 years ago (the code performance now stands at 24 Gflop/s/4-core-CPU, scalable to thousands of CPUs, and we obtain sustained performance over 1 Tflop/s on our small local cluster daily). Second, we exploit the fact that explicit computation is roughly as efficient as implicit computation when Mach numbers are around 1/30.

The code scales to hundreds of thousands of processor cores, for which runs with the proper heating rates, the full convection zone, and well resolved entrainment at the convection zone boundary are easily carried out in a single day.

## TIME AND LENGTH SCALES

The relevant nuclear burning time scale for the H-ingestion problem is the time scale for a proton to be captured by a  $^{12}\text{C}$ :

$$\tau_{12\text{C}}(p) = \frac{12}{X(^{12}\text{C}) \rho N_a \langle \sigma v \rangle_{^{12}\text{C}(p,\gamma)}}.$$

For the quantitative evaluation of the relevant time scales we use the pre-ingestion model at time  $t_0$  shown in Fig. 2 (Sect. 3.2). The mass fraction of  $^{12}\text{C}$  in that model is  $X(^{12}\text{C}) = 0.36$  and the density increases from  $\rho_{\text{top}} = 1.26 \times 10^2 \text{g/cm}^3$  at the top of the convection

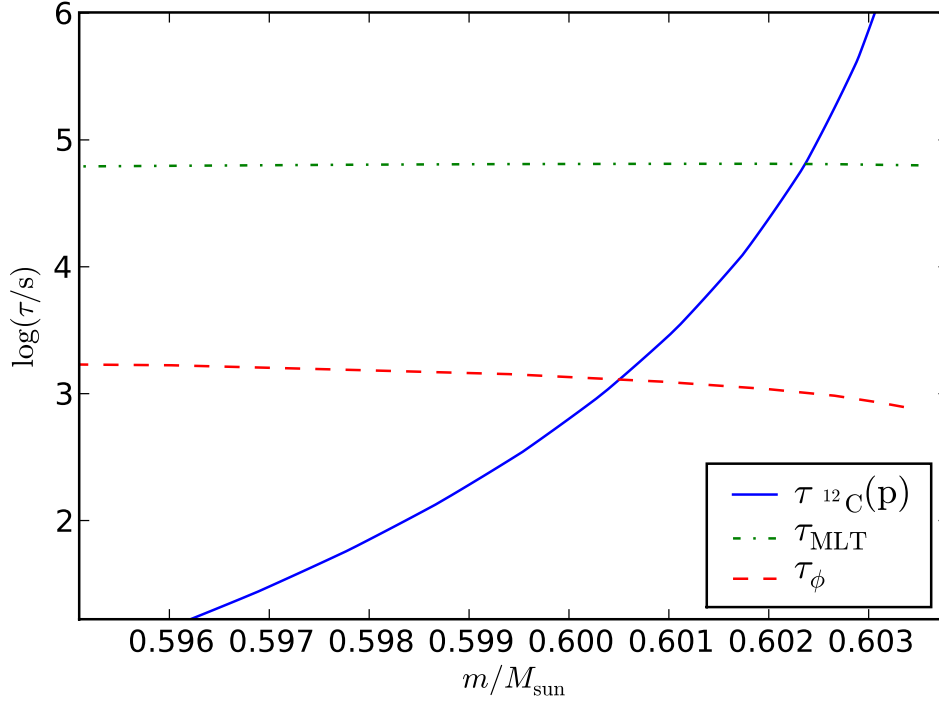


FIG. B13.— Time scales as a function of the mass coordinate in the convection zone, for proton capture by  $^{12}\text{C}$  (blue solid line), as well as the MLT mixing time scale (green dash-dot) and the rate of reaction mixing time scale (red dashed) (see text for details). For this figure the tabulated reaction rate from (Angulo et al. 1999) was used.

zone to  $\rho_{\text{bot}} = 1.0410 \times 10^4 \text{ g/cm}^3$  at the bottom of the convection zone. The nuclear reaction rate  $\langle \sigma v \rangle_{^{12}\text{C}(\text{p},\gamma)}$  depends sensitively on the temperature which increases from  $T_{\text{top}} = 2.2 \times 10^7 \text{ K}$  at the top to  $T_{\text{bot}} = 2.9 \times 10^8 \text{ K}$  at the bottom of the convection zone.  $\langle \sigma v \rangle_{^{12}\text{C}(\text{p},\gamma)}$  increases by 12 orders of magnitude across the convection zone.

The location of the peak H-burning due to H-ingestion takes place where the mixing time scale is the same as  $\tau_{^{12}\text{C}(\text{p})}$  (Ch. 4 Arnett 1996). The diffusion coefficient  $D_{\text{MLT}}$  for convective mixing is derived from the mixing-length theory (MLT). With an appropriate length scale  $l$  a mixing time scale can be obtained. For some properties the MLT mixing-length  $l_{\text{MLT}}$  should be used:  $l_{\text{MLT}} = \alpha_{\text{MLT}} H_{\text{p}}$  with  $\alpha_{\text{MLT}} = 1.7$  the mixing-length parameter and  $H_{\text{p}}$  the pressure scale height. This MLT mixing time scale is then  $\tau_{\text{MLT}} = l_{\text{MLT}}^2 / D_{\text{MLT}}$ . As can be seen in Fig. B13  $\tau_{^{12}\text{C}(\text{p})} = \tau_{\text{MLT}}$  at  $m_{\text{r}} = 0.6024 M_{\odot}$ , a significantly larger mass coordinate than the location of the peak H-burning ( $\sim 0.6005 M_{\odot}$ ) calculated in the stellar evolution model, as evident from the H-profile at  $t_1$  in Fig. 2.

$l_{\text{MLT}}$  should not be used to estimate a mixing time scale relevant for rapid nuclear burning, since the rate of p-captures depends only indirectly on  $P$ . In fact, in the vicinity of the H-peak luminosity the pressure scale height is  $H_{\text{p}} \sim 1.4 \text{ Mm}$  which implies  $l_{\text{MLT}} \sim 2.4 \text{ Mm}$ . This is much larger than the distance over which the rate of p-capture by  $^{12}\text{C}$  (rate of reaction) increases significantly. It is this rate of reaction length scale that defines the width and location of the combustion flame for a given diffusion coefficient. A generalized length for any quantity  $\phi = \phi(r)$  may be defined as (Chapman 1961)

$$H_{\phi} = \frac{1}{\frac{d \ln \phi}{dr}}$$

where  $H_{\phi}$  is the rate of reaction length scale if we define  $\phi = \rho N_{\text{a}} \langle \sigma v \rangle_{^{12}\text{C}(\text{p},\gamma)}$ . The rate of reaction mixing time scale is then  $\tau_{\phi} = H_{\phi}^2 / D_{\text{MLT}}$ . As shown in Fig. B13 the mass coordinate where  $\tau_{^{12}\text{C}(\text{p})} = \tau_{\phi}$  coincides very well with the location of peak H-burning (where as a result the mixing split occurs) at  $t = t_1$  in Fig. 2.

At this location ( $m_{\text{r}} \sim 0.6005 M_{\odot}$ ) the reaction length scale is  $H_{\phi} \sim 330 \text{ km}$  which is the geometric scale of the flame that hydrodynamic simulations including nuclear burn have to resolve. A simulation box that fits the  $4\pi$  geometry of the entire He-shell flash convection zone needs to have a side length of  $50 \text{ Mm}$  which corresponds to  $\sim 166$  flame widths. In order to resolve the flame with at least 10 radial zones an equidistant grid for a H-ingestion flash simulation needs to have a  $1660^3$  grid.